POLISH

ACADEMY

OF SCIENCES

INSTITUTE

OF FUNDAMENTAL

TECHNOLOGICAL

RESEARCH

in cooperation with:

NATIONAL
ENGINEERING   POZNAN
SCHOOL   UNIVERSITY
OF METZ   OF TECHNOLOGY

ENGINEERING TRANSACTIONS

ROZPRAWY INŻYNIERSKIE – TRAITE d'INGENIERIE

WARSZAWA – METZ – POZNAŃ 2014

Faster online: http://et.ippt.pan.pl

ENGINEERING TRANSACTIONS

ROZPRAWY INŻYNIERSKIE – TRAITE d'INGENIERIE

Address of the Editorial Office:
    Engineering Transactions
    Institute of Fundamental Technological Research
    Pawińskiego 5B
    PL 02-106 Warsaw, Poland
    Phone: (48-22) 826 12 81 ext. 206, Fax: (48-22) 826 98 15
    E-mail: engtrans@ippt.pan.pl

SUBSCRIPTIONS

Subscription orders for all journals edited by Institute of Fundamental Technological Research (IPPT) may be sent directly to the Publisher: Institute of Fundamental Technological Research e-mail: subscribe@ippt.pan.pl

Please transfer the subscription fee to our bank account:
Payee: IPPT PAN
Bank: Pekao S.A. IV O/Warszawa
Account number 05124010531111000004426875.

WARUNKI PRENUMERATY

Prenumeratę na wszystkie czasopisma wydawane przez Instytut Podstawowych Problemów Techniki PAN przyjmuje Dział Wydawnictw IPPT.

Bieżące numery Engineering Transactions można nabyć bezpośrednio w Redakcji:
ul. Pawińskiego 5B, 02-106 Warszawa
Tel.: (48-22) 826 60 22; Fax: (48-22) 826 98 15
e-mail: subscribe@ippt.pan.pl

Three years have passed since we started a fruitful cooperation editing the Quarterly Journal ENGINEERING TRANSACTIONS together with the National Engineering School of Metz – ENIM, France. I would like to express thanks and gratitude for the permanent support and interest in this undertaking from the side of the director of ENIM – professor Pierre CHEVRIER as well as for the efforts of the co-editor professor Alexis RUSINEK. Without their contribution the editing of the twelve issues of the Journal with scientific papers from many countries would be not possible.

In this way our Quarterly, founded in 1952 by Witold NOWACKI, Wacław OLSZAK, and Witold WIERZBICKI and appearing since 1953, has been set on a new path of development in its 60 year history. Starting with this issue our cooperation has been enriched by a third partner – one of the best and most dynamically developing technical universities in Poland: the Poznan University of Technology. Professor Tomasz ŁODYGOWSKI – the Rector of PUT declared the intention of active cooperation in editing our Quarterly. Our partners in Poznan closed a local scientific journal: Journal of Civil and Environmental Engineering of its own tradition of editing valuable scientific papers and technical reports for 12 years to concentrate on publishing in ENGINEERING TRANSACTIONS. Having in mind a large number of young scientists working at the PUT as well as predicting the snowball effect regarding other technical universities in Poland, such a decision will enhance the editorial situation of our Quarterly.

Ryszard Pęcherski
Editor

Thermodynamic Method for Measuring the B/A Nonlinear Parameter Under High Pressure

Piotr KIEŁCZYŃSKI[1)], Marek SZALEWSKI[1)], Andrzej BALCERZAK[1)],
Krzysztof WIEJA[1)], Aleksander J. ROSTOCKI[2)],
Ryszard M. SIEGOCZYŃSKI[2)]

[1)] *Institute of Fundamental Technological Research*
Polish Academy of Sciences

Pawińskiego 5B, 02-106, Warszawa, Poland
e-mail: pkielczy@ippt.pan.pl

[2)] *Warsaw University of Technology*
Faculty of Physics

Koszykowa 75, 00-662 Warszawa, Poland

The nonlinearity parameter B/A is a measure of the nonlinearity of the equation of state for a fluid. The nonlinearity parameter B/A is a physical parameter often used in acoustics, from underwater acoustics to biology and medicine. It can provide information about structural properties of the medium, internal pressure and inter-molecular spacing. The thermodynamic method has been applied for determination of B/A parameter in diacylglycerol (DAG) oil as a function of pressure at various temperatures. Isotherms of the density and phase velocity of longitudinal ultrasonic wave as a function of pressure have been measured. Using the thermodynamic method along with measured isotherms of sound speed and density, the nonlinearity parameter B/A (for DAG oil) was evaluated as a function of pressure (up to 220 MPa) at various temperatures ranging from 20 to 50°C.

Key words: nonlinearity parameter B/A, thermodynamic method, high pressure, longitudinal ultrasonic wave velocity.

1. Introduction

The nonlinearity parameter B/A is a measure of the nonlinearity of the equation of state for a fluid. It plays a significant role in acoustics, from underwater acoustics to biology and medicine. The nonlinearity parameter is important because it determines distortion of a finite amplitude wave propagating in the fluid. The parameter B/A determines the nonlinear correction to the velocity due to the influence of nonlinear effects caused by the propagation of finite amplitude wave. Moreover, it can be related to the molecular dynamics of the medium

and it can provide information about structural properties of medium, internal pressures, clustering, and inter-molecular spacing, etc. Importance of the B/A parameter increases with the development of high-pressure technologies of food processing and preservation.

The parameter B/A is very important in medical applications of ultrasound, both in diagnosis and therapy. In diagnostic applications knowledge of B/A is necessary in design and optimization of the ultrasound imaging devices. In therapy it enables to predict the temperature in the tissue during ultrasonic hyperthermia treatment. During nonlinear wave propagation the harmonic frequencies are generated and they are absorbed more quickly than the fundamental one [1, 2].

The experimental techniques for the B/A parameter measurement can be classified by the two basic approaches: thermodynamic method and finite-amplitude method. In the first method, B/A is evaluated from the definition using measurements of the sound velocity as a function of pressure and temperature [3–8]. The second method is based on the analysis of waveform distortion due to harmonics generation during wave propagation [9]. Thermodynamic method is more reliable method for measuring the nonlinearity parameter B/A [10].

The aim of this work is to determine the nonlinearity parameter B/A for DAG (diacylglycerol) oil as a function of hydrostatic pressure and temperature by applying the thermodynamic method [3–8], that uses the measured isotherms of the density and sound velocity in DAG oil.

The authors applied thermodynamic method to determine B/A parameter in diacylglycerol (DAG) oil composed of 82% of DAGs and 18% of triacylglycerols (TAGs), with a vestigial amount of monoacylglycerols (MAGs) and free fatty acids. The fractions were determined by means of the gas chromatography method. DAG oil is an important compound of fatty food products, e.g. vegetable oils [11] and solid animal fats. DAG oil is also applied in the pharmaceutical industry. The consumption of DAG oil is claimed to have beneficial effects on obesity and weight related disorders [12].

In the thermodynamic method to evaluate the nonlinearity parameter B/A one must know (from experiment) the dependence of the longitudinal ultrasonic wave phase velocity on hydrostatic pressure at various temperatures (isotherms). Moreover, one should measure isotherms of the density of a liquid versus pressure. The measurement of sound speed can be performed relatively easily with high accuracy. This is an advantage of the employed thermodynamic method to evaluate the nonlinearity parameter B/A.

The authors have carried out the measurement of isotherms of the longitudinal ultrasonic wave velocity as a function of pressure employing the established laboratory measuring setup. To evaluate the sound velocity in DAG oil, an ultrasonic method that uses cross-correlation method to determine the time-of-flight

between successive impulses was employed. The density of DAG oil was determined from changes of DAG oil sample volume evaluated by measuring the piston displacement in the high-pressure chamber. Consequently, we evaluated the dependence of the nonlinearity parameter B/A on pressure (from atmospheric up to 220 MPa) and temperature (from 20 to 50°C).

2. THEORETICAL BACKGROUND

Expanding the equation of state $P = P(\rho, s)$, (which links pressure P, density ρ and entropy s) of a liquid into a Taylor series along the isentrope $s = s_0$, yields [3]:

$$(2.1) \qquad P - P_0 = A \left(\frac{\rho'}{\rho_0} \right) + \frac{B}{2!} \left(\frac{\rho'}{\rho_0} \right)^2 + \frac{C}{3!} \left(\frac{\rho'}{\rho_0} \right)^3 + \dots,$$

where $\rho' = \rho - \rho_0$ is the excess density, P and ρ are instantaneous pressure and density of the liquid disturbed by the ultrasonic wave propagation, P_0 and ρ_0 are their unperturbed (ambient) values, and

$$(2.2) \qquad A = \rho_0 \left(\frac{\partial P}{\partial \rho} \right)_s \bigg]_{\rho = \rho_0} \equiv \rho_0 c_0^2,$$

$$(2.3) \qquad B = \rho_0^2 \left(\frac{\partial^2 P}{\partial \rho^2} \right)_s \bigg]_{\rho = \rho_0},$$

$$(2.4) \qquad C = \rho_0^3 \left(\frac{\partial^3 P}{\partial \rho^3} \right)_s \bigg]_{\rho = \rho_0},$$

where s is specific entropy, c_0 is the isentropic small-signal sound speed, the partial derivatives are evaluated at the unperturbed state (ρ_0, s_0), what is indicated by the subscript 0. Subscript "s" refers to a constant entropy process, to which the phenomenon of ultrasound propagation can be attributed.

According to the definitions in Eqs. (2.2) and (2.3), the nonlinearity parameter B/A (that is the ratio of quadratic to linear term in the Taylor series expansion) can be expressed as:

$$(2.5) \qquad \frac{B}{A} = \frac{\rho_0}{c_0^2} \left(\frac{\partial^2 P}{\partial \rho^2} \right)_s \bigg]_{\rho = \rho_0}.$$

Using the definition of the sound speed $c^2 = \left(\frac{\partial P}{\partial \rho} \right)_s$, the formula (2.5) can be rewritten as:

$$(2.6) \qquad \frac{B}{A} = 2 \rho_0 c_0 \left(\frac{\partial c}{\partial P} \right)_s \bigg]_{\rho = \rho_0}.$$

Upon expanding the derivative $\left(\dfrac{\partial c}{\partial P}\right)_s\Big]_{\rho=\rho_0}$ we arrive at the following formula [3]:

$$(2.7) \qquad B/A = 2\rho_0 c_0 \left(\frac{\partial c}{\partial P}\right)_T\Big]_{\rho=\rho_0} + 2c_0 T \alpha_p c_p^{-1}\left(\frac{\partial c}{\partial T}\right)_P\Big]_{\rho=\rho_0},$$

where ρ_0 is the density of undisturbed medium, c_0 is the sound velocity for acoustic waves of infinitesimal amplitude, c is the measured sound velocity at given temperature and pressure, P is the pressure, T is the temperature in Kelvin, α_p is the isobaric thermal expansion coefficient, c_p is the isobaric specific heat capacity.

The contribution to B/A parameter from temperature changes is always smaller than that from pressures changes [3].

3. Measuring method and setup

As can be seen from Eq. (2.7), to determine B/A parameter it is necessary to measure accurately sound velocity in the investigated liquid medium as a function of pressure and temperature.

The measuring setup is presented in Fig. 1 and described in [13, 14]. High pressure was generated in a thick-walled cylinder chamber with a simple piston and Bridgman II sealing system. The piston-cylinder assembly was working with a hydraulic press, driven by a hand-operated pump. The piston displacement was controlled by a digital caliper.
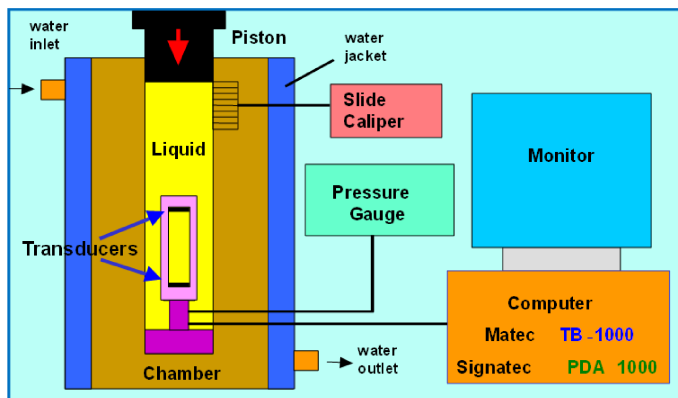
FIG. 1. Experimental ultrasonic setup for measuring the sound velocity in liquids at high pressure and various values of temperature. Temperature of water is stabilized by refrigerated/heating circulator (not presented in the graph).

For pressure measurements a typical 100 Ω manganin transducer was used. Its resistance was measured with a linear unbalanced resistance bridge. The tem-

perature in the chamber was measured using T-type thermocouple (Cu-constantan). A thermostatic bath was circulating in a thermostatic jacket around the chamber. The thermostatic jacket was connected to a precision thermostat. The applied measuring setup and method provided high measurement accuracy.

The accuracy of measurements of ultrasonic wave phase velocity depends on the level of parasitic ultrasonic signals. For measurements of the phase velocity of longitudinal ultrasonic waves, the authors have developed and constructed the computerized setup especially designed to obtain a low level of parasitic ultrasonic signals. A special mounting of transducers in the high-pressure chamber was fabricated. The transducers were operating in the through transmission mode. The transmitting transducer was driven by the TB-1000 pulser – receiver computer card. Ultrasonic pulses (5 MHz sine-wave trains) were generated by the transmitting transducer and detected by the receiving transducer. The PDA-1000 digitizer card sampled and digitized the signals received by the transducer and amplified by the receiver. The stored signals were then analyzed by computer software.

The transducers were separated by the distance L. The time of flight of the ultrasonic pulses was evaluated by applying the cross-correlation method. Measurement of the time of flight of the ultrasonic pulses is difficult and uncertain applying classical methods. Therefore, it is more favorable to use methods based on digital signal processing, e.g. cross-correlation method [15]. The cross-correlation function $h(t)$, of two functions of time, $f(t)$ and $g(t)$, is defined as follows:

$$(3.1) \qquad h(t) = \int\limits_{-\infty}^{+\infty} f(\tau)g(t+\tau)\,\mathrm{d}\tau.$$

The function $f(t)$ corresponds to the first signal detected by the receiving transducer. This is the ultrasound pulse that travels once across the distance L between the transmitting and receiving transducers. Part of the ultrasonic energy of the first signal is reflected at the receiving transducer back to the transmitting transducer, which in turn reflects part of the incident energy back to the receiving transducer. As a result, the next impulse detected by the receiving transducer (function $g(t)$) will travel an extra distance $2L$ between the transducers. Hence, this signal travels the distance $3L$. The correlation analysis gives a measure of the similarity between two considered pulses $f(t)$ and $g(t)$ shifted in time. These two pulses have a similar shape but a different amplitude and delay. Therefore, the cross-correlation function reaches a maximum for t equal to the evaluated time difference corresponding to the distance $2L$. The time of flight was measured with a nanosecond resolution. For each measure-

ment, the ultrasonic signal was averaged 1024 times in order to improve the signal-to-noise ratio.

The sound velocity was measured with the expanded relative uncertainty equal to ±0.3% at 95% confidence level. The expanded relative uncertainty of the density measurements amounts to ±0.05%.

4. RESULTS

4.1. *Experimental results and discussion*

4.1.1. Sound velocity. In the DAG oil high-pressure phase transitions occur [16]. As the temperature raises, the pressure at which the phase transition begins increases. At 20°C phase transition starts at a pressure of 220 MPa, at a temperature of 30°C the phase transition starts at a pressure of 300 MPa, etc. For this reason, the calculation of nonlinearity parameter value B/A was performed only for the low-pressure phase of DAG oil, in the pressure range from atmospheric pressure up to a pressure of 220 MPa. Determination of the parameter of nonlinearity required to carry out measurements of velocity and density isotherms in the DAG oil.

Figure 2 shows the results of longitudinal ultrasonic wave velocity measurements (frequency 5 MHz) at temperatures: 20, 30, 40, 50°C. Pressure was applied in increments of 10 MPa up to 220 MPa. Each increase in pressure was followed by an interval of time (5 min), which allowed the DAG oil to achieve the thermodynamic equilibrium conditions.
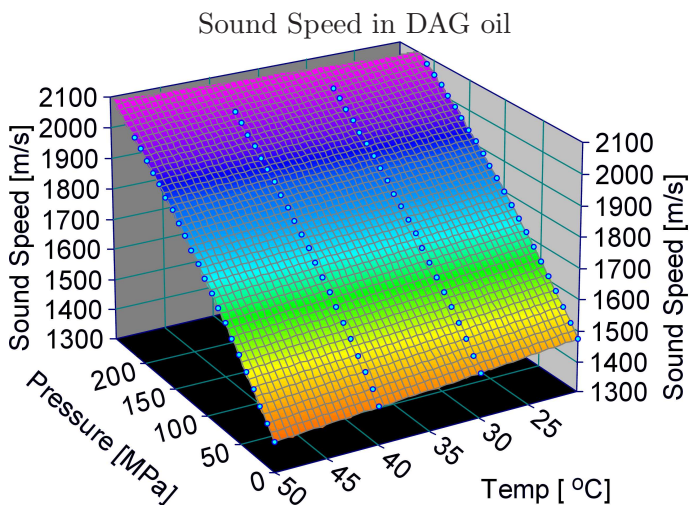
FIG. 2. Plots of sound speed in DAG oil as a function of pressure along various isotherms ($T = 20, 30, 40,$ and $50°C$), $f = 5$ MHz.

4.1.2. Density. Figure 3 shows the dependence of the density of DAG oil versus pressure and temperature in the case of low-pressure phase. During experiments, DAG oil volume changes were measured by observation of piston displacement inside the high-pressure chamber. It was measured by a digital caliper gauge. Corrections related to the expansion of the chamber were considered during data analysis. Density values of DAG oil under high pressure were evaluated from the measurements of the DAG oil sample volume, i.e., $\rho(p,T) = m/V(p,T)$, where m is the mass of the sample, and $V(p,T)$ is the sample volume at pressure p and temperature T.
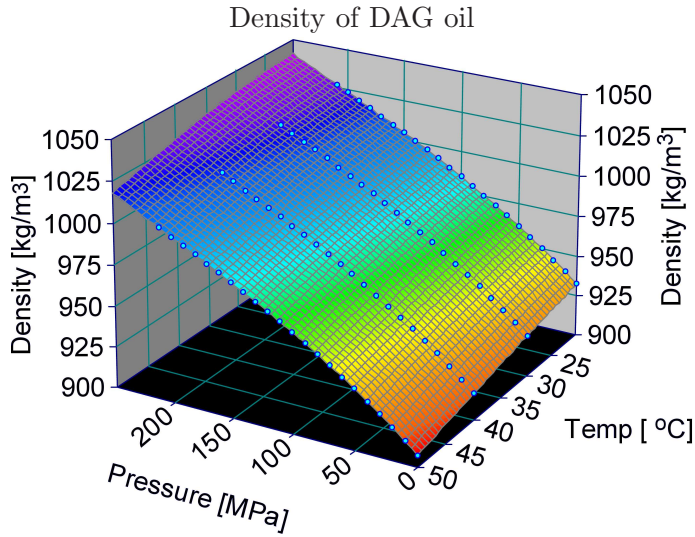
FIG. 3. Density of DAG oil as a function of pressure and temperature.

4.2. Numerical evaluation of the B/A parameter

Empirical relationships $c(p,T)$ and $\rho(p,T)$ have been approximated by the appropriate functions of two variables (p,T), i.e., the pressure p and the temperature T. Computer software package Table Curve 3D (Systat, USA) was used to perform the curve fittings. Sound velocity was approximated by using a third order polynomial of two independent variables (p,T):

$$(4.1) \quad c(p,T) = a + bp + cT + dp^2 + eT^2 + fpT + gp^3 + hT^3 + ipT^2 + jpT^2,$$

where $a = 1556.1007$, $b = 3.5558133$, $c = -5.2591231$, $d = -0.0046743392$, $e = 0.070266476$, $f = 0.0082758464$, $g = 3.8777839e{-}6$, $h = -0.0005704745$, $i = -3.0256387e{-}5$, $j = -9.7492135e{-}6$.

Similar approximation was also performed for the density $\rho(p,T)$ of DAG oil.

4.2.1. *Pressure-dependent term B/A' of the nonlinearity parameter B/A.*

$$(4.2) \qquad B/A' = 2\rho_0 c_0 \left(\frac{\partial c}{\partial P} \right)_T \Bigg]_{\rho=\rho_0},$$

where $\rho_0 = 930.17 \ \text{kg/m}^3$, $c_0 = 1473.30 \ \text{m/s}$.

In order to calculate the dependence of the B/A' on the pressure and temperature, one should calculate the derivative of the speed of sound with respect to the pressure at a constant temperature.

4.2.2. *The temperature-dependent term B/A''.*

$$(4.3) \qquad B/A'' = 2c_0 T \alpha_p c_p^{-1} \left(\frac{\partial c}{\partial T} \right)_P \Bigg]_{\rho=\rho_0}.$$

Evaluation of the parameter B/A'' required the calculation of the temperature derivative of the speed of sound. Furthermore, the thermal expansion coefficient α_p and specific heat capacity at constant pressure c_p had to be calculated, namely:

$$(4.4) \qquad \alpha_p(p,T) = \frac{-1}{\rho(p,T)} \left(\frac{\partial \rho}{\partial T} \right)_p.$$

Specific heat capacity at constant pressure c_p has been calculated using the following equation:

$$(4.5) \qquad c_p(p,T) = \frac{T \alpha_p^2(p,T)}{\rho(p,T)(k_T - k_s)},$$

where T is the temperature in Kelvin, k_T is the isothermal compressibility, k_s is the adiabatic compressibility.

Isothermal compressibility has been determined from the following formula:

$$(4.6) \qquad k_T(p,T) = \frac{1}{\rho(p,T)} \left(\frac{\partial \rho}{\partial p} \right)_T.$$

Adiabatic compressibility was determined from the expression:

$$(4.7) \qquad k_s(p,T) = \frac{1}{\rho(p,T) c^2(p,T)}.$$

4.2.3. Nonlinearity parameter B/A. Using the results of numerical calculations of the pressure-dependent part B/A' (from Eq. (4.2)), the temperature-dependent part B/A'' (from Eq. (4.3)) and the Eq. (2.7), the nonlinearity parameter B/A values were evaluated as a function of pressure and temperature.

The plots of calculated values of B/A nonlinear parameter as a function of pressure, at temperatures: 20, 30, 40, 50°C are shown in Fig. 4. The derivatives of sound velocity on pressure and temperature were evaluated numerically. B/A nonlinearity parameter has been evaluated in the pressure range before the beginning of the phase transition, for low-pressure phase of DAG oil. The nonlinear parameter B/A depends slightly on the temperature. On the contrary, the pressure dependence of B/A is pronounced. These results are consistent with Beyer's paper [3]. The B/A parameter diminishes quasi-linearly with increasing pressure, see Fig. 4.
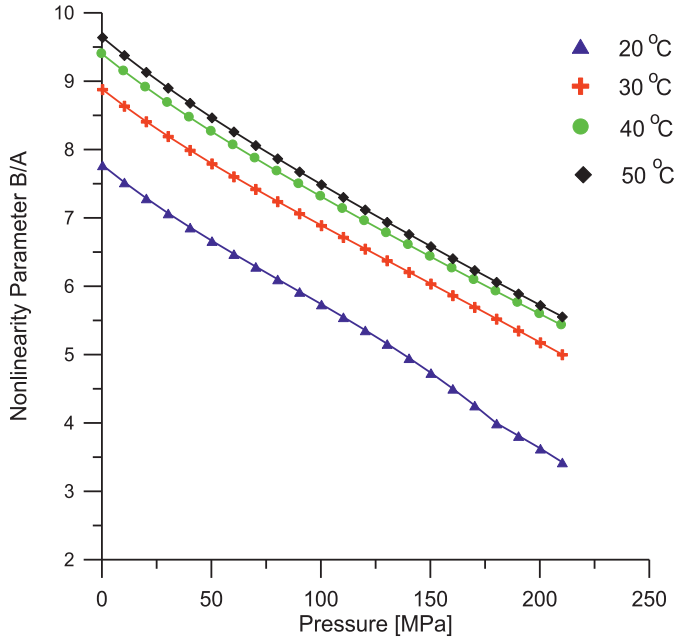
FIG. 4. Nonlinearity parameter B/A as a function of pressure at various temperatures evaluated for the low-pressure phase of DAG oil, ($T = 20, 30, 40,$ and $50°C$).

The second term B/A'' in the formula for the parameter of nonlinearity B/A is negative and gives a smaller contribution to the formula for the overall ratio B/A than the pressure-dependent term B/A'.

To the authors knowledge, evaluation of the B/A nonlinearity parameter in a such broad range of pressures (up to 220 MPa) is a novelty.

5. Conclusions

Usefulness of ultrasonic thermodynamic method to evaluate the nonlinear parameter B/A that employs the measured velocity and density isotherms versus pressure in the investigated liquid was stated. The performed analysis shows a large monotonic decrease of B/A nonlinearity parameter for DAG oil, with increasing pressure. For example, at temperature $t = 50°C$, B/A nonlinearity parameter decreases from 9.7 at atmospheric pressure, to about 5.6 at 210 MPa.

The measuring ultrasonic high-pressure setup and applied procedure have been employed successfully to evaluate the nonlinear parameter B/A for a wide range of pressures and temperatures. The results obtained in this paper can be useful in acoustics, biology, medicine and investigations of materials. Presented in this study method, can also be applied to investigate other liquids, e.g. fuels and biofuels, lubricants, polymers, etc.

Measurements of sound velocity are relatively easy therefore determination of B/A nonlinearity parameter offers a simple way to evaluate the molecular properties of liquids under high pressures at various temperatures. Acoustic nonlinearity is related to the internal pressure, free energy of binding, the effective van der Waals' constants, the translational diffusion coefficient, and the rotational correlation time [17]. This method can be used not only for pure liquids but also for mixtures [18], emulsions and solutions [19].

A number of important thermodynamic parameters of the liquid can be established from measurements of sound speed isotherms as a function of pressure. This will be the subject of future work of the authors.

References

1. Duck F.A., *Nonlinear acoustics in diagnostic ultrasound*, Ultrasound in Medicine and Biology, **28**, 1, 1–18, 2002.

2. Liu X., Gong X., Yin C., Li J., Zhang D., *Noninvasive estimation of temperature elevation in biological tissues using acoustic nonlinearity parameter imaging*, Ultrasound in Medicine and Biology, **34**, 3, 414–424, 2008.

3. Beyer R.T., *Parameter of nonlinearity in fluids*, J. Acoust. Soc Amer., **32**, 719–721, 1960.

4. Zorębski E., Zorębski M., *Acoustic nonlinearity parameter B/A determined by means of thermodynamic method under elevated pressure for alkanediols*, Ultrasonics, **54**, 1, 368–374, 2014.

5. Beyer R.T., *The parameter B/A, in Nonlinear Acoustics*, M.F. Hamilton and D.T. Blackstock [Eds.], Academic Press, New York, 1998.

6. Khelladi H., Plantier F., Daridon J.L., Djelouah H., *Measurement under high pressure of the nonlinearity parameter B/A in glycerol at various temperatures*, Ultrasonics, **49**, 668–675, 2009.

7. COPPENS A.B., BEYER R.T., SEIDEN M.B., DONOHUE J., GUEPIN F., HODSON R.H., TOWNSEND CH., *Parameter of nonlinearity in fluids*, Journal of the Acoustical Society of America, **37**, 797–804, 1965.

8. ZHU Z., ROOS M.S., COBB W.N., JENSEN K., *Determination of the acoustic nonlinearity parameter B/A from phase measurements*, Journal of the Acoustical Society of America, **87**, 5, 797–804, 1983.

9. ADLER L., HIEDEMANN E.A., *Determination of the nonlinearity parameter B/A for water and m-Xylene*, J. Acoust. Soc Amer., **34**, 410–412, 1962.

10. LAW W.K., FRIZZELL L.A., DUNN F., *Comparison of thermodynamic and finite amplitude methods of B/A measurement in biological materials*, J. Acoust. Soc. Amer., **74**, 1295–1297, 1983.

11. SHIMIZU M., KUDO N., NAKAJIMA N., MATSUO Y., KATSARAGI I., TOKIMITSU I., BARCELO I., MATEU C., BARCELO F., *Acidity and DAG content of olive oil recently produced on the Island of Mallorca*, Journal of the American Oil Chemists' Society, **85**, 11, 1051–1056, 2008.

12. LO S.K., TAN C.P., LONG K., YUSOFF M.S.A., LAI O.M., *Diacylglycerol oil – properties, processes and products: A review*, Food Bioprocess. Technol., **1**, 223–233, 2008.

13. ROSTOCKI A.J., SIEGOCZYŃSKI R.M., KIEŁCZYŃSKI P., SZALEWSKI M., BALCERZAK A., ZDUNIAK M., *Employment of a novel ultrasonic method to investigate high pressure phase transitions in oleic acid*, High Press. Res., **31**, 334–338, 2011.

14. KIEŁCZYŃSKI. P., SZALEWSKI M., ROSTOCKI A.J., ZDUNIAK M., SIEGOCZYŃSKI R.M., BALCERZAK A., *Investigation of high-pressure phase transitions in vegetable oils by measuring phase velocity of longitudinal ultrasonic waves*, IEEE Intern. Ultrason. Symp. Proc., pp. 1563–1566, Rome 2009.

15. SUGASAWA S., *Time difference measurement of ultrasonic pulses using cross-correlation function between analytic signals*, Japanese Journal of Applied Physics, **41**, 3299–3307, 2002.

16. KIEŁCZYŃSKI P., SZALEWSKI M., BALCERZAK A., MALANOWSKI A., SIEGOCZYŃSKI R.M., PTASZNIK S., *Investigation of high-pressure phase transitions in DAG (diacylglycerol) oil using the Bleustein-Gulyaev ultrasonic wave method*, Food Res. Int., **49**, 60–64, 2012.

17. SEGHAL C.M., *Non-linear ultrasonics to determine molecular properties of pure liquids*, Ultrasonics, **33**, 155–161, 1995.

18. LU Y., FENG J., DANWU Y., TONG J., *Computation of the acoustic nonlinearity parameter in organic liquid binary mixtures*, Chinese Science Bull., **45**, 414–417, 2000.

19. OAKLEY B.A., BARBER G., WORDEN T., HANNA D., *Ultrasonic parameters as a function of absolute hydrostatic pressure*, Journal of Physical and Chemical Reference Data, **32**, 4, 1501–1544, 2003.

The Use of Computed Tomography and Ultrasonic Imaging for Assessment of Defects in Plates Made of a Polyesteric Resin

Daniela Ioana TUDOR, Stefan Dan PASTRAMA, Anton HADAR

University Politehnica
Department of Strength of Materials
Faculty of Engineering and Management of Technological Systems
Splaiul Independentei 313, Sector 6, 060042, Bucharest, Romania
e-mail: stefan.pastrama@upb.ro

The paper presents an experimental assessment of defects in a layered plate made of a polyesteric resin (plastic material). Two non-destructive methods were used: X-ray computed tomography and ultrasonic imaging. The main purpose of this work was to establish the position, shape and size of the defects that appeared during the manufacturing process. A three – dimensional model was obtained from the X-ray tomography using specific software for data processing. The model was used in order to evaluate the effect of defects on the integrity of the analyzed structure, by comparing the numerical results with the ones for a similar plate without defects. Some considerations on the efficiency of the two used experimental methods are also presented.

Key words: X-ray computed tomography, ultrasonic imaging, finite element method, defects.

1. Introduction

Nowadays, polyesters (plastic materials) tend to replace classic materials in many fields, either due to functional or to economic reasons. In order to produce high performance structures made of plastic materials, it is very important to manufacture them without defects that could affect the behavior in service, otherwise the quality conditions may not be fulfilled. A quantitative evaluation of the possible defects that may appear during the manufacturing process or in service should be performed periodically. Usually, such a check is done by non-destructive methods. *The non-destructive control* represents a type of control in which dismantling or destruction of the structure is not necessary. Nowadays, it plays a very important role in the structural integrity assessment of industrial

parts or assemblies, mainly due to the possibility of detection and measurement of defects. Periodic control avoids premature failure of components with bad or even catastrophic consequences, emphasizing the state of integrity of structures both during the manufacturing process and in service. A very important feature of such methods is the possibility of obtaining information regarding the existence, dimensions and shape of defects. This can be used as input data in numerical calculations regarding the structural integrity or lifetime in service of a component.

Non-destructive methods based on ultrasound properties have seen a spectacular development in the last years. *Ultrasonic imaging* is a non-invasive technique based on the principles of spectral analysis, allowing the user to capture images that can emphasize microstructural details at a scale comparable with the one of metallographic analysis [1, 2]. Ultrasounds propagate on large distances in metallic materials, reflect and/or refract at the interface between two environments with different acoustic impedance. The propagation speed depends on the mass density and Young's modulus of the propagation environment. The most important property of ultrasounds is reflection at the interface of two environments, and in particular, on the surface of a defect. Ultrasound examination is used nowadays for metallic components as laminated semi products, plates, metal sheets, rails, casted, forged or welded products, pipes, tanks, etc. It is used also for measurements of thickness in parts that are accessible only on one side.

The X-ray computed tomography is a non-destructive technique that uses X-rays to obtain 2D images taken around an axis of rotation and digital processing to generate a 3D image of the inside of an object from the 2D images. The 3D reconstruction of the structure can be converted into input data for subsequent numerical analyses using proper software [3].

Several researchers have used these non-destructive methods to assess the structural integrity of machine parts and especially to investigate the initiation and development of cracks.

The automatic detection of internal defects in composite materials using non-destructive techniques is described in [4]. The authors propose two steps for interpreting ultrasonic data: the pre-processing technique necessary to normalize the signals of composite structures with different thicknesses and the classification techniques used to compare the ultrasonic signals and detect classes of similar points. The efficiency of the ultrasonic technique was evaluated by GARNIER *et al.* [5], in the case of detection of in site defects resulting from impact or in-service damages in complex aeronautical structures such as wings or rods. The authors evaluated also two other techniques (InfraRed Thermography and Speckle Shearing Interferometry) in order to find the most suitable one from the point of view of precision and quickness and reported that ultrasonic testing

enables the depth of a defect to be determined while the other two techniques offered a shorter detection time. For improved detection of defects in plastic pipes, and especially when such flaws are close to the interfaces, a new approach in ultrasonic inspection, based on a combined application of non-linear deconvolution and the Hilbert–Huang transform was proposed by KAZYS *et al.* [6]. PAU *et al.* [7], proposed a technique, based on the analysis of the reflection of high frequency ultrasonic waves from the wheel-rail interface, which was used to obtain graphic maps used to determine the shape of the contact area, to measure its size, and also to collect qualitative information about the distribution of the wheel-rail contact pressure.

Microtomography was used in order to evaluate the evolution of cracks in structures made of aluminum alloys casted under pressure [8, 9]. The obtained experimental information was further processed to obtain numerical models aiming at characterizing the initiation of cracks starting from the voids. SCOTT *et al.* [10], used High Resolution Synchrotron Radiation Computed Tomography to detect fiber damage progression in a carbon-epoxy notched laminate loaded to failure. SHARMA *et al.* obtained effective tensile moduli of 3D carbon/carbon composites using image-based finite element simulations and experiments [11]. The non-destructive evaluations were conducted using X-ray tomography in order to explore cracks, voids, and fiber bundles distortion and to reconstruct 3D finite element meshes containing most of these defects. Investigation of defects in fiber-reinforced polymers, textile composites or layered foams using X-ray tomography were described also by other researchers [12–14].

The techniques of ultrasonic imaging and X-ray computed tomography were compared and evaluated to investigate artificial defects made using very small drill bits in aluminum castings [15]. The authors showed that defects smaller than 0.3 mm could not be detected by ultrasonic tests, but could be emphasized using X-ray tomography, without obtaining precise dimensions.

When non-destructive testing is to be used, it is very important to properly establish the most adequate method. The choice is based on several factors, as: type of material, presumed dimensions of the investigated structures, type of defects (surface or embedded), costs, etc.

This paper presents the non-destructive evaluation of a layered plate made of polyesteric resin. Both X-ray computed tomography and ultrasonic imaging were employed in order to establish the position, shape and size of the defects that appeared during manufacturing of the plate. A numerical model was obtained further to the experimental investigations and proper processing of the collected data. The model is presented as an example of how 3D models obtained using non-destructive techniques can be used to evaluate the effect of defects on the integrity of the analyzed structure, by comparing the numerical results with the ones for a similar plate without defects.

2. Experimental work

2.1. The specimen

The analyzed plate was obtained by successive casting of two layers of polyesteric resin and has a rectangular shape (Fig. 1). Each layer has a thickness of 1.3 mm. The purpose of the non-destructive evaluation was to detect possible casting defects at the interface between the layers (lack of adherence, voids, etc.) and to obtain a 3D model of the flawed plate in order to evaluate the mechanical influence of defects using the finite element method.
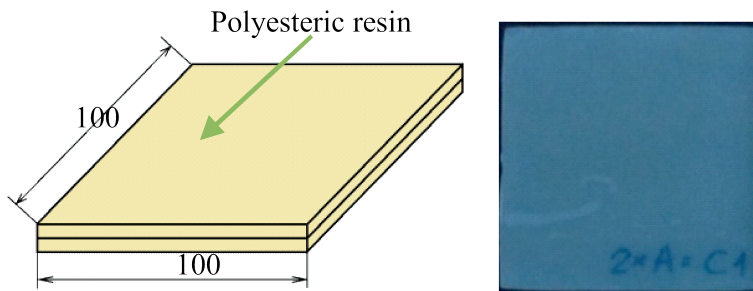
Fig. 1. The specimen.

Two non-destructive methods were used for the assessment of defects, namely X-ray computed tomography and ultrasonic imaging. The use of two procedures was justified on one side by the possibility of validation of some results by comparison between the data yielded from each method and, on the other side, by the limitations of each method. Information obtained from each method can lead to a more precise image of the shape, dimensions and location of the detected defects [16].

2.2. Experimental investigations using X-ray computed tomography

X-ray computed tomography is based on the measurement of the degree of attenuation of the electromagnetic radiation that travels through the examined object and reconstruction of the 3D image of the object using the 2D projections of the cross sections. Through this non-destructive method, one can get important information regarding the materials of the investigated structures and the interior shape, and, last but not least, a 3D reconstruction of the analyzed object can be obtained.

The studied specimen was investigated using a helical CT scan (Fig. 2). High quality images can be very quickly achieved due to the state-of-the art detector technology. The typical CT image is composed of 512 rows, each of 512 pixels.
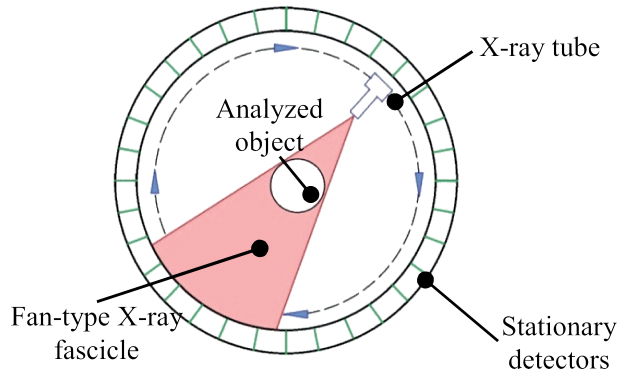
FIG. 2. Working principle of the CT scan.

Results of the scanning procedure were processed using the software eFilm Workstation (trial version) [17], an application used for viewing and manipulating medical images, that works in two consecutive stages: i) the presence, shape, position and dimensions of discontinuities were established first and ii) segmentation of planes was then realized having as final result the 3D reconstruction of the plate.

In the first stage, results were processed using the following steps:

- The 2D sections obtained using X-ray scanning were analyzed and the section with the maximum size of a found defect was chosen;
- Two planes of interest were defined for this section: a horizontal (frontal) and a vertical (sagittal) plane;
- Using the dedicated software and the defined planes, the chosen section is reconstructed in each plane
- In the frontal plane, one can emphasize: the shape of the defect, the overall dimensions of the plate, the dimensions of the defect and the position of the defect in this plane.
- In the sagittal plane, the thickness of the specimen and the depth of the defect are put in evidence.

A series of tomographic images were achieved for the studied plate, emphasizing several defects. The main one was a lack of adherence between the layers with a maximum length $L_{\max} = 37$ mm, a maximum width $W_{\max} = 5$ mm and a maximum depth $h_{\max} = 1.1$ mm. Other defects with smaller dimensions could be observed on the tomographic images (Fig. 3).

The second stage is dedicated to the processing of the 2D slices in order to reconstruct the 3D image of the specimen. This model was further used in the numerical simulations in order to establish the influence of defects on the in-service behavior of the structure. Here, the following steps were undertaken:
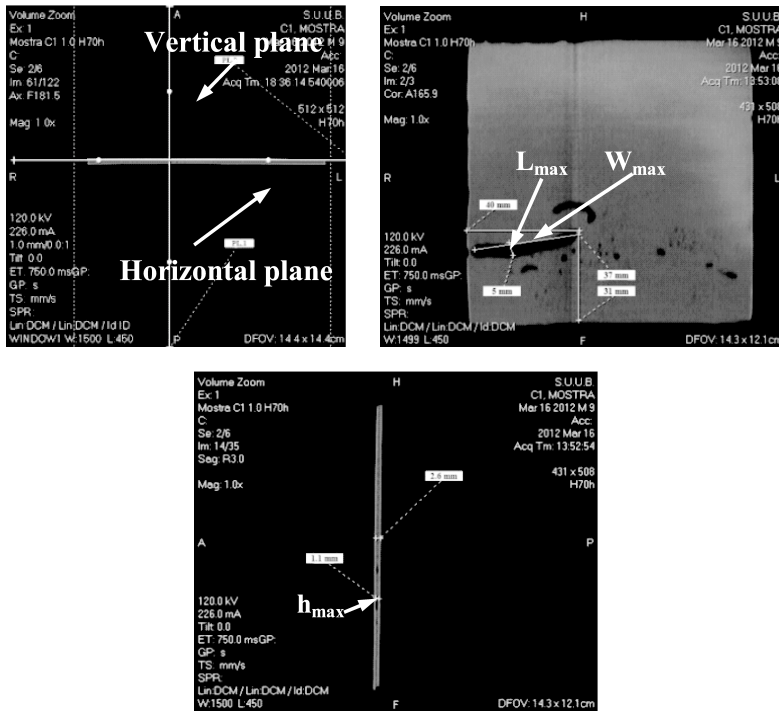
FIG. 3. Processing of the tomographic images.

- Calibration of the 2D images obtained following the X-ray scan;
- Definition of objects through the attenuation coefficient;
- Definition of regions of interest;
- Auto segmentation of the surfaces, based on the differences between the mass densities (shades of grey from the images);
- Reconstruction of the 3D volume using segmented surfaces.

The reconstructed object is shown in Fig. 4.

FIG. 4. The reconstructed volume.

2.3. *Experimental investigations using ultrasonic imaging*

The second step of this research is the analysis of the studied plate using ultrasonic imaging. For this purpose, an equipment Nuclear MicroSonic-01 was used. The experimental set-up, shown in Fig. 5, is a complex equipment for automatic ultrasonic examination of rectangular or cylindrical samples in order to detect and characterize flaws in the analyzed structure [18]. The equipment allows ultrasonic examination with different incidence angles, both using longitudinal and transversal waves. The area under examination is automatically scanned with a high resolution ultrasonic fascicle, using mechanical devices for displacement and a data acquisition system for amplitude and flight time data, measured on the echo signals, synchronous with the scanning of the investigated domain. The obtained data, saved in amplitude and time of flight files depending on the used coordinates (circumferential or radial) allow construction of C-scan or B-scan ultrasonic images of the scanned area. From the pair of C-scan representation in amplitude and time of flight corresponding to each incident angle, a B-scan representation depth of defect – radial position can be achieved for a section through the sample. Such images are extremely useful since they contain all information regarding the found defects: shape, dimensions and orientation.

Fig. 5. The experimental set-up for ultrasonic imaging.

The considered plate was analyzed by ultrasonic imaging in the following conditions: immersion in demineralized water through automatic scanning of bottom echo and defect echo. A flaw detector USIP12-Krautkramer type A312 with the nominal frequency of 10MHz was used. The ultrasonic images of the detected defects are presented as amplitude image (Fig. 6) and time of flight image (Fig. 7).
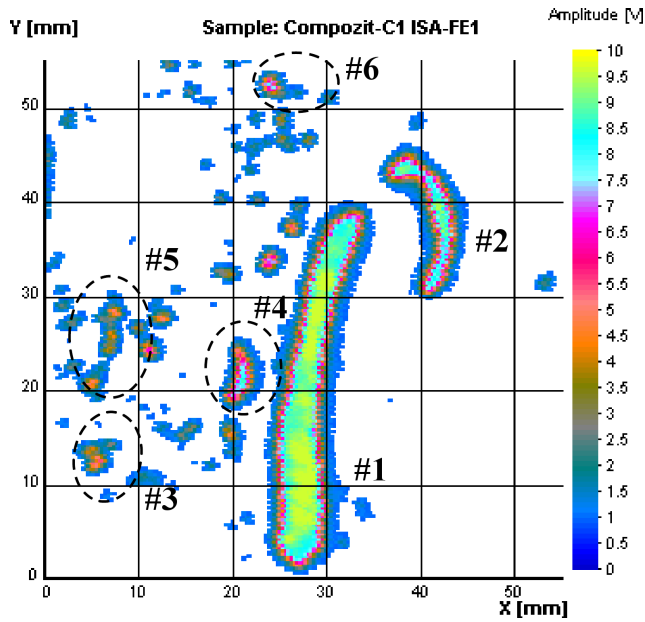
Fig. 6. Ultrasonic image in amplitude.
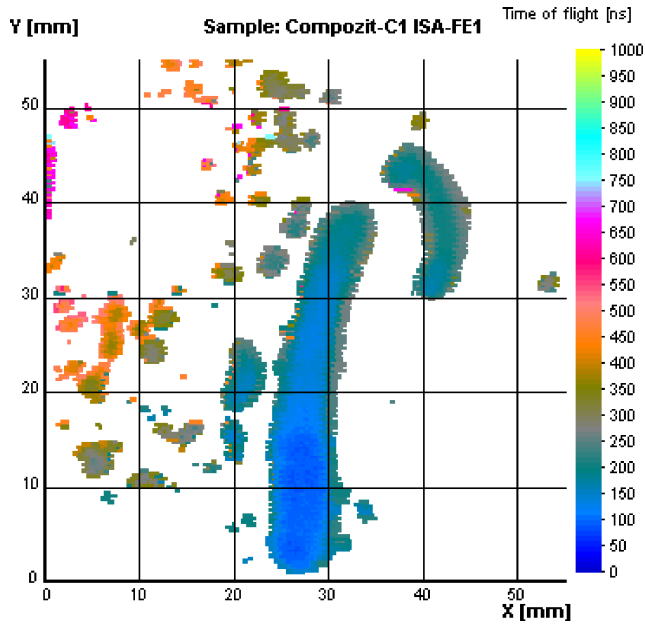
Fig. 7. Ultrasonic image in time of flight.

The image in amplitude was used to measure the position and dimensions of defects while the image in time of flight was used to obtain the depth of defects.

In this way, a characterization of all defects in the plate was achieved in terms of position and dimensions. The results for the six defects emphasized in Fig. 6 are presented in Table 1.

Table 1. Position and dimensions of defects.

No.	Position		Dimensions		
	X-coordinate [mm]	Y-coordinate [mm]	Length on X [mm]	Length on Y [mm]	Depth [mm]
1	24.6–33.6	1.7–39.0	9.0	37.3	1.2–1.5
2	36.6–43.5	30.6–45.1	6.9	14.5	1.3–1.5
3	19.2–22.2	18.8–24.5	3.0	5.7	1.3–1.4
4	23.1–24.9	33.1–34.9	1.8	1.8	1.4–1.5
5	6.0–8.4	24.0–29.1	2.4	5.1	1.6–1.8
6	23.1–25.2	51.5–53.3	21	1.8	1.4–1.6

Analyzing the dimensions of the most important defect (No. 1) on can see that its span on the OY axis, found using ultrasonic imaging (37.3 mm) is very close to the length determined by X-ray computed tomography (37 mm). Also, dimensions and position of other defects, with smaller importance were obtained.

3. Numerical results

The 3D reconstruction of the studied plate using X-ray tomography was used further in order to obtain a numerical model, analyzed with the finite element method [16]. The two biggest defects (No. 1 and No. 2) were taken into account and inserted in the 3D model (Fig. 8). Also, a calibration model (without defects) was analyzed in order to compare the stresses in order to assess the influence of the considered defects on the mechanical behavior of the plate.
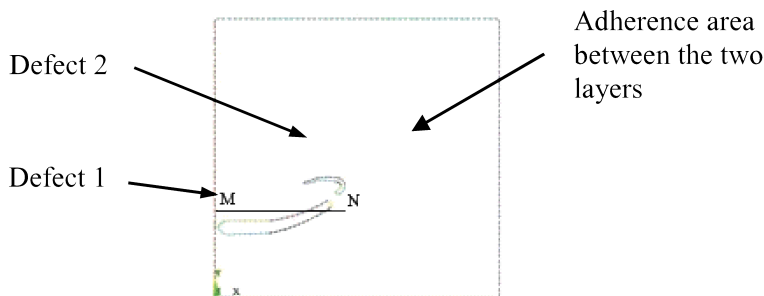
Fig. 8. The 3D model obtained from reconstruction.

Before the numerical analysis, a traction test was performed in order to establish the stress-strain curve of the considered plastic material. A universal INSTRON 8801 testing machine was used for testing nine specimens with rectangular cross section at room temperature and with a rate of 0.1 mm/min. The results were averaged, resulting the stress-strain curve from Fig. 9. Although in the studied literature referring to the CT-scans of samples made of or containing polymers [10–14] it was not found any mention to the possible modifications of the mechanical characteristics due to X-ray exposure, the authors verified this hypothesis. For this, after the CT-scan tests, specimens made of the material of the scanned plate were manufactured and tested in traction. Differences from the stress-strain curve of the material between the non-exposed and exposed specimens were insignificant, showing thus that the influence of the X-ray exposure on the mechanical characteristics of the used material is negligible.
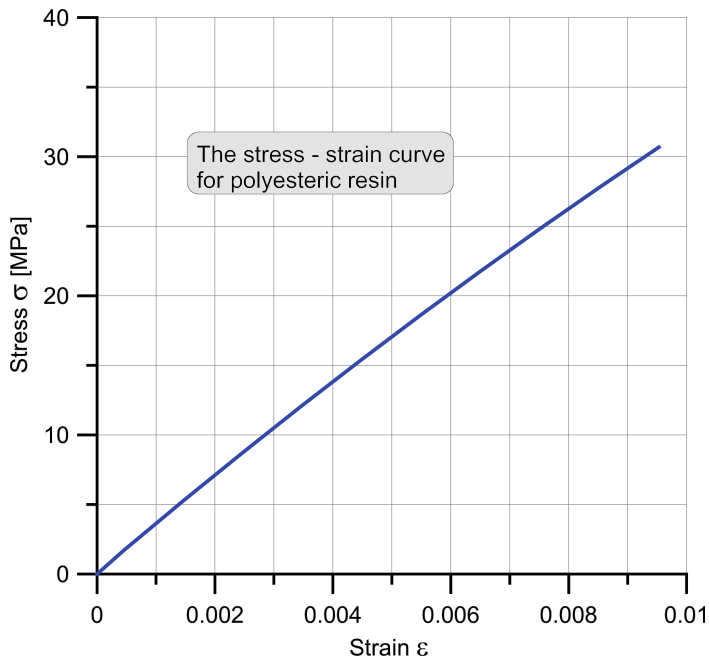
FIG. 9. The average stress-strain curve of the polyesteric resin.

A Young's modulus of 3482.2 MPa was obtained by drawing the tangent to the curve in origin. Since a small non-linearity can be observed on the curve, data obtained from the tensile test were inserted in the input file of the finite element study in order to perform a non-linear analysis. A common loading case was considered for the layered plate: bending load through a uniformly

distributed force for the plate simply supported on the edges. For this loading case, both the flawed and the calibration plate were analyzed using a model with eight nodded isoparametric solid elements. Both plates contained the same number of nodes and elements, the difference in the two meshes being only the fact that, for the plate with defects, the nodes were decoupled in the area of discontinuities in order to simulate two independent surfaces and to model thus the lack of adherence between the layers. The finite element model is shown in Fig. 10.
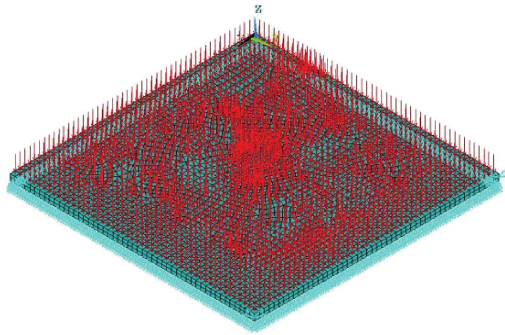
FIG. 10. The finite element model.

The most interesting results in terms of stresses are those for the middle section that is at the bonded surfaces of the two plates, where the defects were discovered at the non-destructive tests. The map of the von Mises equivalent stress in the middle section is presented in Fig. 11 for both the flawed and calibration plate. It should be mentioned that the contour maps are presented with values of the stress in non-dimensional form σ_{eq}/p_0 where p_0 is the applied uniform pressure, whose absolute value was chosen as to yield stresses lower than the 0.2 offset yield limit found from the stress-strain curve.

a)

b)
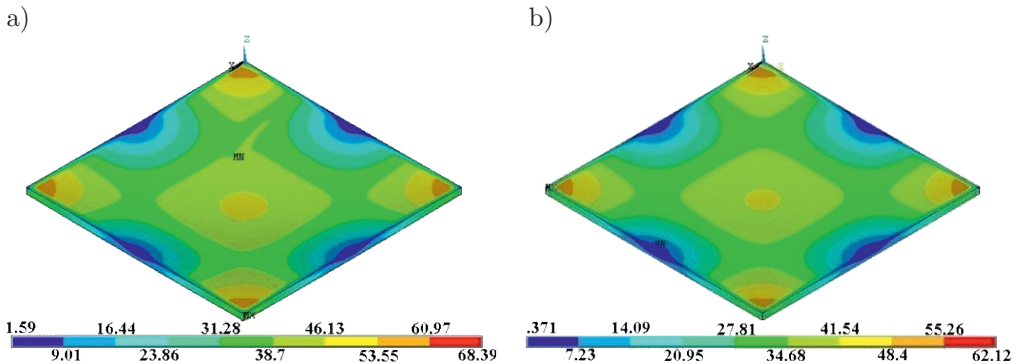
FIG. 11. Contour map of the non-dimensional von Mises equivalent stress: a) flawed plate, b) calibration plate.

A comparative graph of variation of the non-dimensional equivalent von Mises stress σ_{eq}/p_0 in the middle section, on a line passing through the most important defect (line MN in Fig. 8) is presented in Fig. 12. The variation is plotted as a function of the non-dimensional length x/L where x is the distance from point M on the line MN and L is the total length of the plate.
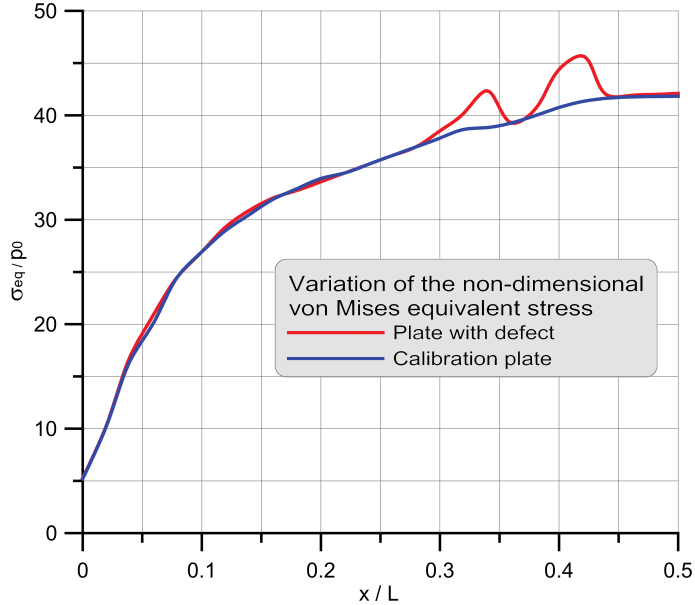
FIG. 12. Comparative variation of the von Mises equivalent stress in the middle section on line MN.

Analysis of the obtained results revealed that the discovered defects produced an increase of the maximum stress in the plate with about 10% but the defect is not dangerous in the sense that the increase does not affect the carrying capacity of the structure. Also, the plot from Fig. 12 shows that in the area of defect, the stresses in the flawed plate are about 10% bigger than those in the calibration plate. This difference appears for the non-dimensional length x/L between 0.3 ... 0.45 this means where the line MN intersects the defect. Such stress concentration is small and, consequently, the growth of the flaw is unlikely to appear.

4. CONCLUSIONS

The present paper describes an experimental evaluation of the manufacturing defects in a casted two-layer plate made of a polyesteric resin. Two non-destructive methods were used: X-ray computed tomography and ultrasonic

imaging. Thus, the presence, shape and position of macro defects in the analyzed structure were established.

The first method allowed for a 3D reconstruction of the plate and detection of some defects (lack of adherence between the layers). Also, the dimensions of the bigger defects were obtained. The exact characterization of defects using this method is not easy, but a good approximation of their position and dimensions is achieved. The most important advantage of the X-ray computed tomography is the possibility of 3D reconstruction of the studied structures, with all important defects that appear during manufacturing or in service.

Using the ultrasonic imaging, position and dimensions of the most important but also of other smaller defects were emphasized with greater precision. The main dimension of the bigger defect was found in the ultrasonic amplitude image with a difference of less than 0.1% compared to the dimension found with computed tomography. Thus, the 3D model obtained through X-ray tomography can be corrected.

In the paper, an example of use of the reconstructed volume through X-ray tomography in a numerical analysis is also presented. The corrected reconstructed 3D volume of the specimen with the major defects taken into account was used in a non-linear finite element analysis that is an example of how such experimental results may be further used to predict the possible influences of the discovered defects on the carrying capacity of the analyzed structure.

Finally, it should be emphasized that, for a correct prediction of the in service behavior and of the carrying capacity of a structure, the periodic non-destructive evaluation is very important. In this way, defects that may appear in the manufacturing process or in service can be detected. Also, the use of X-ray computed tomography enables the possibility of reconstruction of the volume which can be further used as input data in a numerical analysis that can give a picture of the influence of the defects on the behavior of the structure. Thus, the engineer may take the decision to repair the structure or to continue to use it without the possibility of failure.

5. Acknowledgements

References

1. BLITZ J., SIMPSON G., *Ultrasonic Methods of Non-destructive Testing*, Champman & Hall, London, UK, 1996.

2. ENSMINGER D., BOND L., *Ultrasonics – Fundamentals, Technologies and Application*, CRC Press, New York, 2011.

3. SEERAM E., *Computed tomography – Physical Principles, Clinical Applications and Quality Control*, third edition, Saunders Elsevier, St. Louis, Missouri, 2009.

4. D'ORAZIO T., LEO M., DISTANTE A., GUARAGNELLA C., PIANESE V., CAVACCINI G., *Automatic ultrasonic inspection for internal defect detection in composite materials*, NDT&E International, **41**, 145–154, 2008.

5. GARNIER C., PASTOR M.-L., EYMA F., LORRAIN B., *The detection of aeronautical defects in situ on composite structures using Non Destructive Testing*, Composite Structures, **93**, 1328–1336, 2011.

6. KAZYS R., TUMSYS O., PAGODINAS D., *Ultrasonic detection of defects in strongly attenuating structures using the Hilbert-Huang transform*, NDT&E International, **41**, 457–466, 2008.

7. PAU M., LEBAN B., BALDI A., *Simultaneous subsurface defect detection and contact parameter assessment in a wheel-rail system*, Wear, **265**, 1837–1847, 2008.

8. FERRIE E., BUFFIERE J.Y., LUDWIG W., *3D characterisation of the nucleation of a short fatigue crack at a pore in a cast Al alloy using high resolution synchrotron microtomography*, International Journal of Fatigue, **27**, 1215–1220, 2005.

9. VANDERESSE N., MAIRE É., CHABOD A., BUFFIÈRE J.Y., *Microtomographic study and finite element analysis of the porosity harmfulness in a cast aluminium alloy*, International Journal of Fatigue, **33**, 1514–1525, 2011.

10. SCOTT A.E., MAVROGORDATO M., WRIGHT P., SINCLAIR I., SPEARING S.M., *In situ fibre fracture measurement in carbon-epoxy laminates using high resolution computer tomography*, Composites Science and Technology, **71**, 1471–1477, 2011.

11. SHARMA R., MAHAJAN P., KUMAR MITTAL R., *Elastic modulus of 3D carbon/carbon composite using image-based finite element simulations and experiments*, Composite Structures, **98**, 69–78, 2013.

12. WIESAUER K., PIRCHER M., GOTZINGER E., HITZENBERGER C.K., OSTER R., STIFTER D., *Investigation of glass–fibre reinforced polymers by polarisation-sensitive, ultra-high resolution optical coherence tomography: Internal structures, defects and stress*, Composites Science and Technology, **67**, 3051–3058, 2007.

13. BLACKLOCK M., BALE H., BEGLEY M., COX B., *Generating virtual textile composite specimens using statistical data from micro-computedtomography: 1D tow representations for the Binary Model*, Journal of the Mechanics and Physics of Solids, **60**, 451–470, 2012.

14. HUA Z.W., DE CARLO F., *Noninvasive three-dimensional visualization of defects and crack propagation in layered foam structures by phase-contrast microimaging*, Scripta Materialia, **59**, 1127–1130, 2008.

15. CHO I.S., HWANG J.H., YANG S.M., LIM C.H., *Evaluation of defects in aluminum piston castings by using ultrasonics and computer tomography*, China Foundry, **9**, 3, 275–278, 2012.

16. TUDOR D.I., *Contributii privind evaluarea cantitativa a influentei defectelor de material asupa capacitatii portante a unor structuri – (Contributions regarding the quantitative evaluation of the influence of material defects on the carrying capacity of some structures)* (in Romanian) – PhD Thesis, University Politehnica of Bucharest, 2012.

17. * * * eFilm Workstation$^{\circledR}$ – User Guide, Merge Healthcare Incorporated, 2010.

18. SOARE M., *Performance Characterization of Nondestructive Methods for Flow Detection and Sizing in CANDU Pressure Tubes. Part. I: Ultrasonic Spectroscopy Investigation Using Longitudinal Waves for Interrogation*, NNDT Report no. RCD-ICC-AIEA-27.1/2001, Nuclear NDT Research & Services, Bucharest, Romania, 2001.

An Alternative Approach of Initial Stability Analysis of Kirchhoff Plates by the Boundary Element Method

Michał GUMINIAK

Poznan University of Technology

Piotrowo 5, 60-965 Poznań, Poland
e-mail: michal.guminiak@put.poznan.pl

An initial stability of Kirchhoff plates is analysed in the paper. Proposed approach avoids Kirchhoff forces at the plate corner and equivalent shear forces at a plate boundary. Two unknown variables are considered at the boundary element node. The governing integral equations are derived using Betti theorem. The integral equations have the form of boundary and domain integral equations. The constant type of boundary element are used. The singular and non-singular formulation of the boundary-domain integral equations with one and two collocation points associated with a single boundary element located at a plate edge are presented. To establish a plate curvature by double differentiation of basic boundary-domain integral equation, a plate domain is divided into rectangular sub-domains associated with suitable collocation points. A plate curvature can also be establish by considering three collocation points located in close proximity to each other along line pararel to one of the two axes of global coordinate system and establishment of appropriate differential operators.

Key words: the boundary element method, Kirchhoff plates, initial stability, fundamental solution.

1. INTRODUCTION

The Boundary Element Method (BEM) is one of many tools applied to the numerical analysis of structures. The main advantage of BEM is its relative simplicity of formulating and solving problems of the potential theory and the theory of elasticity. Many authors applied the boundary element method in wide aspects to static, dynamic and stability analysis of plates. BURCZYŃSKI [1] described in a comprehensive manner the boundary element method and its application in a variety of fields, the theory of elasticity together with the appropriate solutions and a discussion of the basic types of boundary elements. The BEM found a wide application in the analysis of plates too. There are well known works of ALTIERO

and SIKARSKIE [2], BÈZINE and GAMBY [3] and STERN [4] applied the boundary element method to solve the plate bending problem. The direct boundary element method in plate bending was applied by HARTMANN and ZOTEMANTEL [5]. Comparisaon of the effectiveness of the boundary element method with the finite element method and application of the BEM in the analysis of thick plates was done by DEBBIH [6, 7]. The evaluation of boundary integrals for thin plate bending analysis was proposed by ABDEL-AKHER and HARTLEY [8]. HARTLEY [9] also proposed the plate bending theory for frame structures analysis. BESKOS [10] and WEN, ALIABADI and YOUNG [11] applied the BEM in the dynamic analysis of plates. ALIABADI and WROBEL [12] described an application of BEM in the thick plate analysis together with procedures for calculating singular and hypersingular integrals. A number of contributions devoted to the analysis of plates were presented by: KATSIKADELIS [13, 14], KATSIKADELIS and YOTIS [15], KATSIKADELIS, SAPOUNTZAKIS and ZORBA [16], KATSIKADELIS and KANDILAS [17], KATSIKADELIS and SAPOUNTZAKIS [18]. SHI [19] applied BEM formulation for vibration and initial stability problem of orthotropic thin plates. In order to simplify the calculation procedures GUMINIAK, OKUPNIAK and SYGULSKI [20] proposed a modified formulation of the boundary integral equation for a thin plate. This approach was extended for static, dynamic and stability analysis of thin plates and it is presented together with several numerical examples in many papers, e.g. [21–25]. MYŚLECKI [26, 27] proposed BEM to static analysis of plane girders and BEM combined with approximate fundamental solutions for problem of plate bending resting on elastic foundation. Author used non-singular approach of boundary integral equations wherein the derivation of the second boundary integral equation was executed for additional collocation points located outside of a plate domain. The same approach of derivation of boundary integral equation was proposed by MYŚLECKI and OLEŃKIEWICZ [28, 29] to free vibration analysis of thin plates. Authors also used isoparametric, three-node boundary elemnt and applied dual reciprocity principle to dermine the inertia forces inside a plate domain. Very interesting approach was presented by LITEWKA and SYGULSKI [30, 31] who applied the GANOWICZ [32] fundamental solutions for Reissner plates to static analysis of plates. KATSIKADELIS [33] applied BEM in a wide aspects of engineering analysis of plates.

In classic form the BEM is limited to linear problems with known fundamental solutions. To fully overcomes this drawback the conception of the Analog Equation Method (AEM) was created and introduced by KATSIKADELIS [34]. This version of BEM is basing on formulation of boundary-domain integral equation method and can treat efficiently not only linear problems, whose fundamental solution can not be established or it is difficult to treat numerically, but also nonlinear differential equations and systems of them as well. The method

is based on the principle of the analog equation of Katsikadelis for differential equations. This conception was established to analysis of plate buckling by NERANTZAKI and KATSIKADELIS [35] and CHINNABOON, CHUCHEEPSAKUL and KATSIKADELIS [36]. Similarly BABOUSKOS and KATSIKADELIS [37, 38] solved problem of flutter instability of dumped plate subjected by conservative and non-conservative loading. A wide review of literature devoted to application of BEM in plate analysis takes place in work of GUMINIAK and LITEWKA [39]. Authors compared thin [20, 21] and thick (Reissner) [30, 31] plate theory in therms of the modified BEM formulation and application of Ganowicz fundamental solutions [32]. Additionally, in the paper [39] the analysis of plate resting on internal flexible supports and plate with variable thickness in terms of AEM were presented.

In present paper, an analysis of plate initial stability the BEM will be presented. The analysis will focus on the modified [23] formulation of thin plate bending. The BÈZINE [3] technique will be established to directly derive boundary-domain integral equation.

2. INTEGRAL FORMULATION OF PLATE BENDING AND INITIAL STABILITY PROBLEM

The differential equation qoverning of plate initial stability has the form [40, 41]:

$$(2.1) \qquad D \cdot \nabla^4 w = -\overline{p},$$

where p is the substitute load, which has the form:

$$(2.2) \qquad \overline{p} = N_x \cdot \frac{\partial^2 w}{\partial x^2} + 2N_{xy} \cdot \frac{\partial^2 w}{\partial x \partial y} + N_y \cdot \frac{\partial^2 w}{\partial y^2}.$$

In the majority of contributions devoted to the application of BEM to the thin (Kirchhoff) plate theory, the derivation of the boundary integral equation involves the known boundary variables of the classic plate theory, i.e. the shear force and the concentrated corner forces. Thus, on the plate boundary there are considered the two physical quantities: the equivalent shear force V_n, reaction at the plate k-th corner R_k, the bending moment M_n, the corner concentrated forces and two geometric variables: the displacement w_b and the angle of rotation in the normal direction φ_n. The boundary integral equation can be derived using the Betti's theorem. Two plates are considered: an infinite plate, subjected to the unit concentrated force and a real one, subjected to the real in plane loadings N_x, N_{xy} and N_y. The plate bending problem is described in a unique

way by two boundary-domain integral equations. The first equation has the form:

$$(2.3)\ c(\mathbf{x})\cdot w(\mathbf{x})+\int_{\Gamma}[V_n^*(\mathbf{y},\mathbf{x})\cdot w_b(\mathbf{y})-M_n^*(\mathbf{y},\mathbf{x})\cdot\varphi_n(\mathbf{y})]\cdot d\Gamma(\mathbf{y})-\sum_{k=1}^{K}R^*(k,\mathbf{x})\cdot w(k)$$

$$=\int_{\Gamma}[V_n(\mathbf{y})\cdot w^*(\mathbf{y},\mathbf{x})-M_n(\mathbf{y},\mathbf{x})\cdot\varphi_n^*(\mathbf{y},\mathbf{x})]\cdot d\Gamma(\mathbf{y})-\sum_{k=1}^{K}R_k\cdot w^*(k,\mathbf{x})$$

$$+\int_{\Omega}\left(N_x\cdot\frac{\partial^2 w}{\partial x^2}+2N_{xy}\cdot\frac{\partial^2 w}{\partial x\partial y}+N_y\cdot\frac{\partial^2 w}{\partial y^2}\right)\cdot w^*(\mathbf{y},\mathbf{x})\cdot d\Omega(\mathbf{y}),$$

where the fundamental solution of this biharmonic equation

$$(2.4)\qquad\qquad\qquad\nabla^4 w^*(\mathbf{y},\mathbf{x})=\frac{1}{D}\cdot\delta(\mathbf{y},\mathbf{x})$$

which is the free space Green function given as

$$(2.5)\qquad\qquad\qquad w^*(\mathbf{y},\mathbf{x})=\frac{1}{8\pi D}\cdot r^2\cdot\ln(r)$$

for a thin isotropic plate, $r=|\mathbf{y}-\mathbf{x}|$, δ is the Dirac delta, $D=\dfrac{E\,h^3}{12(1-v^2)}$ is the plate stiffness, $\mathbf{x}$ is the source point and $\mathbf{y}$ is a field point. The coefficient $c(\mathbf{x})$ is taken as:

$c(\mathbf{x})=1$, when $\mathbf{x}$ is located inside the plate domain,
$c(\mathbf{x})=0.5$, when $\mathbf{x}$ is located on the smooth boundary,
$c(\mathbf{x})=0$, when $\mathbf{x}$ is located outside the plate domain.

The second boundary-domain integral equation can be obtained replacing the unit concentrated force $P^*=1$ by the unit concentrated moment $M_n^*=1$. Such a replacement is equivalent to the differentiation of the first boundary integral equation (2.3) with respect to the co-ordinate n at a point $\mathbf{x}$ belonging to the plate domain and letting this point approach the boundary and taking n coincide with the normal to it. The resulting equation has the form:

$$(2.6)\ c(\mathbf{x})\cdot\varphi_n(\mathbf{x})+\int_{\Gamma}\left[\overline{V}_n^*(\mathbf{y},\mathbf{x})\cdot w_b(\mathbf{y})-\overline{M}_n^*(\mathbf{y},\mathbf{x})\cdot\varphi_n(\mathbf{y})\right]\cdot d\Gamma(\mathbf{y})-\sum_{k=1}^{K}\overline{R}^*(k,\mathbf{x})\cdot w(k)$$

$$=\int_{\Gamma}[V_n(\mathbf{y})\cdot\overline{w}^*(\mathbf{y},\mathbf{x})-M_n(\mathbf{y})\cdot\overline{\varphi}_n^*(\mathbf{y},\mathbf{x})]\cdot d\Gamma(\mathbf{y})-\sum_{k=1}^{K}R_k\cdot\overline{w}^*(k,\mathbf{x})$$

$$+\int_{\Omega}\left(N_x\cdot\frac{\partial^2 w}{\partial x^2}+2N_{xy}\cdot\frac{\partial^2 w}{\partial x\partial y}+N_y\cdot\frac{\partial^2 w}{\partial y^2}\right)\cdot\overline{w}^*(\mathbf{y},\mathbf{x})\cdot d\Omega(y),$$

where

$$\left\{\overline{V}_n^*(\mathbf{y},\mathbf{x}),\overline{M}_n^*(\mathbf{y},\mathbf{x}),\overline{R}^*(\mathbf{y},\mathbf{x}),\overline{w}^*(\mathbf{y},\mathbf{x}),\overline{w}^*(\mathbf{y},\mathbf{x}),\overline{\varphi}_n^*(\mathbf{y},\mathbf{x})\right\}$$

$$= \frac{\partial}{\partial n(\mathbf{x})}\left\{V_n^*(\mathbf{y},\mathbf{x}),M_n^*(\mathbf{y},\mathbf{x}),R^*(k,\mathbf{x}),w^*(k,\mathbf{x}),w^*(\mathbf{y},\mathbf{x}),\varphi_n^*(\mathbf{y},\mathbf{x})\right\}.$$

The second boundary-domain integral equation can be also derived by introducing additional collocation point, which is located in the same normal line outside the plate edge. According this approach, the second equation has the same mathematical form as the first one (2.3). This double collocation point approach was presented in publication [27–29].

The detailed procedure for the derivation of the fundamental solution, the integral representation of the solution and the two boundary-domain integral equations is presented by Katsikadelis in [33]. The issues related to the assembly of the algebraic equations in terms of the classical boundary element method are discussed in many papers, including [33].

The plate bending problem can also be formulated in a modified, simplified way using an integral representation of the plate biharmonic equation. Because the concentrated force at the corner is used only to satisfy the differential biharmonic equation of the thin plate, one can assume, that it could be distributed along a plate edge segment close to the corner. Hence, the terms in the boundary integral Eqs. (2.5) and (2.6) which correspond to the corner force R can be substituted in the following way:

$$(2.7) \qquad -\sum_{k=1}^{K} R_k \cdot w^*(k,\mathbf{x}) = \int_{\Gamma_k} R_n(\mathbf{y}) \cdot w^*(\mathbf{y},\mathbf{x}) \cdot \mathrm{d}\Gamma_k(\mathbf{y}),$$

$$(2.8) \qquad -\sum_{k=1}^{K} R_k \cdot \overline{w}^*(k,\mathbf{x}) = \int_{\Gamma_k} R_n(\mathbf{y}) \cdot \overline{w}^*(\mathbf{y},\mathbf{x}) \cdot \mathrm{d}\Gamma_k(\mathbf{y}),$$

where the subscript k denotes an unknown segment of the plate edge near the corner. In the Eqs. (2.7) and (2.8) the fundamental twisting moment $M_{ns}^*(\mathbf{y})$ must be considered, too. Hence, the boundary integral equations will take the form:

$$(2.9) \quad c(\mathbf{x})\cdot w(\mathbf{x})+\int_{\Gamma}[T_n^*(\mathbf{y},\mathbf{x})\cdot w(\mathbf{y})-M_n^*(\mathbf{y},\mathbf{x})\cdot\varphi_n(\mathbf{y})-M_{ns}^*(\mathbf{y},\mathbf{x})\cdot\varphi_s(\mathbf{y})]\cdot\,\mathrm{d}\Gamma(\mathbf{y})$$

$$= \int_{\Gamma}[T_n(\mathbf{y})\cdot w^*(\mathbf{y},\mathbf{x})-M_n(\mathbf{y})\cdot\varphi_n^*(\mathbf{y},\mathbf{x})]\cdot\mathrm{d}\Gamma(\mathbf{y})+\int_{\Gamma_k}R_n(\mathbf{y})\cdot w^*(\mathbf{y},\mathbf{x})\cdot\mathrm{d}\Gamma_k(\mathbf{y})$$

$$+\int_{\Omega}\left(N_x\cdot\frac{\partial^2 w}{\partial x^2}+2N_{xy}\cdot\frac{\partial^2 w}{\partial x\partial y}+N_y\cdot\frac{\partial^2 w}{\partial y^2}\right)\cdot w^*(\mathbf{y},\mathbf{x})\cdot\mathrm{d}\Omega(\mathbf{y}),$$

$$(2.10) \quad c(\mathbf{x}) \cdot \varphi_n(\mathbf{x}) + \int_\Gamma \left[\overline{T}_n^*(\mathbf{y}, \mathbf{x}) \cdot w(\mathbf{y}) - \overline{M}_n^*(\mathbf{y}, \mathbf{x}) \cdot \varphi_n(\mathbf{y}) - \overline{M}_{ns}^*(\mathbf{y}, \mathbf{x}) \cdot \varphi_s(\mathbf{y}) \right] \cdot d\Gamma(\mathbf{y})$$

$$= \int_\Gamma \left[T_n(\mathbf{y}) \cdot \overline{w}^*(\mathbf{y}, \mathbf{x}) - M_n(\mathbf{y}) \cdot \overline{\varphi}_n^*(\mathbf{y}, \mathbf{x}) \right] \cdot d\Gamma(\mathbf{y})$$

$$+ \int_{\Gamma_k} R_n(\mathbf{y}) \cdot \overline{w}^*(\mathbf{y}, \mathbf{x}) \cdot d\Gamma_k(\mathbf{y}) + \int_\Omega \left(N_x \cdot \frac{\partial^2 w}{\partial x^2} + 2N_{xy} \cdot \frac{\partial^2 w}{\partial x \partial y} + N_y \cdot \frac{\partial^2 w}{\partial y^2} \right)$$

$$\cdot \overline{w}^*(\mathbf{y}, \mathbf{x}) \cdot d\Omega(\mathbf{y}).$$

Because the length k of the plate edge segment is unknown, the selected components of the Eqs. (2.9) and (2.10) can form a common integral:

$$(2.11) \quad c(\mathbf{x}) \cdot w(\mathbf{x}) + \int_\Gamma [T_n^*(\mathbf{y}, \mathbf{x}) \cdot w(\mathbf{y}) - M_n^*(\mathbf{y}, \mathbf{x}) \cdot \varphi_n(\mathbf{y}) - M_{ns}^*(\mathbf{y}, \mathbf{x}) \cdot \varphi_s(\mathbf{y})] \cdot d\Gamma(\mathbf{y})$$

$$= \int_\Gamma [T_n(\mathbf{y}) \cdot w^*(\mathbf{y}, \mathbf{x}) + R_n(\mathbf{y}) \cdot w^*(\mathbf{y}, \mathbf{x}) - M_n(\mathbf{y}) \cdot \varphi_n^*(\mathbf{y}, \mathbf{x})] \cdot d\Gamma(\mathbf{y})$$

$$+ \int_\Omega \left(N_x \cdot \frac{\partial^2 w}{\partial x^2} + 2N_{xy} \cdot \frac{\partial^2 w}{\partial x \partial y} + N_y \cdot \frac{\partial^2 w}{\partial y^2} \right) \cdot w^*(\mathbf{y}, \mathbf{x}) \cdot d\Omega(\mathbf{y}),$$

$$(2.12) \quad c(\mathbf{x}) \cdot \varphi_n(\mathbf{x}) + \int_\Gamma \left[\overline{T}_n^*(\mathbf{y}, \mathbf{x}) \cdot w(\mathbf{y}) - \overline{M}_n^*(\mathbf{y}, \mathbf{x}) \cdot \varphi_n(\mathbf{y}) - \overline{M}_{ns}^*(\mathbf{y}, \mathbf{x}) \cdot \varphi_s(\mathbf{y}) \right] \cdot d\Gamma(\mathbf{y})$$

$$= \int_\Gamma [T_n(\mathbf{y}) \cdot \overline{w}^*(\mathbf{y}, \mathbf{x}) + R_n(\mathbf{y}) \cdot \overline{w}^*(\mathbf{y}, \mathbf{x}) - M_n(\mathbf{y}) \cdot \overline{\varphi}_n^*(\mathbf{y}, \mathbf{x})] \cdot d\Gamma(\mathbf{y})$$

$$+ \int_\Omega \left(N_x \cdot \frac{\partial^2 w}{\partial x^2} + 2N_{xy} \cdot \frac{\partial^2 w}{\partial x \partial y} + N_y \cdot \frac{\partial^2 w}{\partial y^2} \right) \cdot \overline{w}^*(\mathbf{y}, \mathbf{x}) \cdot d\Omega(\mathbf{y}).$$

Then, the common factor $w*$ can be separated:

$$(2.13) \quad c(\mathbf{x}) \cdot w(\mathbf{x}) + \int_\Gamma [T_n^*(\mathbf{y}, \mathbf{x}) \cdot w(\mathbf{y}) - M_n^*(\mathbf{y}, \mathbf{x}) \cdot \varphi_n(\mathbf{y}) - M_{ns}^*(\mathbf{y}, \mathbf{x}) \cdot \varphi_s(\mathbf{y})] \cdot d\Gamma(\mathbf{y})$$

$$= \int_\Gamma [(T_n(\mathbf{y}) + R_n(\mathbf{y})) \cdot w^*(\mathbf{y}, \mathbf{x}) - M_n(\mathbf{y}) \cdot \varphi_n^*(\mathbf{y}, \mathbf{x})] \cdot d\Gamma(\mathbf{y})$$

$$+ \int_\Omega \left(N_x \cdot \frac{\partial^2 w}{\partial x^2} + 2N_{xy} \cdot \frac{\partial^2 w}{\partial x \partial y} + N_y \cdot \frac{\partial^2 w}{\partial y^2} \right) \cdot w^*(\mathbf{y}, \mathbf{x}) \cdot d\Omega(\mathbf{y}),$$

$$(2.14) \quad c(\mathbf{x})\cdot\varphi_n(\mathbf{x})+\int_\Gamma\left[\overline{T}^*_n(\mathbf{y},\mathbf{x})\cdot w(\mathbf{y})-\overline{M}^*_n(\mathbf{y},\mathbf{x})\cdot\varphi_n(\mathbf{y})-\overline{M}^*_{ns}(\mathbf{y},\mathbf{x})\cdot\varphi_s(\mathbf{y})\right]\cdot d\Gamma(\mathbf{y})$$

$$= \int_\Gamma [(T_n(\mathbf{y}) + R_n(\mathbf{y}))\cdot\overline{w}^*(\mathbf{y},\mathbf{x}) - M_n(\mathbf{y})\cdot\overline{\varphi}^*_n(\mathbf{y},\mathbf{x})]\cdot d\Gamma(\mathbf{y})$$

$$+ \int_\Omega\left(N_x\cdot\frac{\partial^2 w}{\partial x^2} + 2N_{xy}\cdot\frac{\partial^2 w}{\partial x\partial y} + N_y\cdot\frac{\partial^2 w}{\partial y^2}\right)\cdot\overline{w}^*(\mathbf{y},\mathbf{x})\cdot d\Omega(\mathbf{y}).$$

Now, the new notation is introduced:

$$(2.15) \qquad\qquad \widetilde{T}_n(\mathbf{y}) = T_n(\mathbf{y}) + R_n(\mathbf{y}).$$

Hence, the boundary integral equations will have the form:

$$(2.16) \quad c(\mathbf{x})\cdot w(\mathbf{x})+\int_\Gamma[T^*_n(\mathbf{y},\mathbf{x})\cdot w(\mathbf{y})-M^*_n(\mathbf{y},\mathbf{x})\cdot\varphi_n(\mathbf{y})-M^*_{ns}(\mathbf{y},\mathbf{x})\cdot\varphi_s(\mathbf{y})]\cdot d\Gamma(\mathbf{y})$$

$$= \int_\Gamma\left[\widetilde{T}_n(\mathbf{y})\cdot w^*(\mathbf{y},\mathbf{x}) - M_n(\mathbf{y})\cdot\varphi^*_n(\mathbf{y},\mathbf{x})\right]\cdot d\Gamma(\mathbf{y})$$

$$+ \int_\Omega\left(N_x\cdot\frac{\partial^2 w}{\partial x^2} + 2N_{xy}\cdot\frac{\partial^2 w}{\partial x\partial y} + N_y\cdot\frac{\partial^2 w}{\partial y^2}\right)\cdot w^*(\mathbf{y},\mathbf{x})\cdot d\Omega(\mathbf{y}),$$

$$(2.17) \quad c(\mathbf{x})\cdot\varphi_n(\mathbf{x})+\int_\Gamma\left[\overline{T}^*_n(\mathbf{y},\mathbf{x})\cdot w(\mathbf{y})-\overline{M}^*_n(\mathbf{y},\mathbf{x})\cdot\varphi_n(\mathbf{y})-\overline{M}^*_{ns}(\mathbf{y},\mathbf{x})\cdot\varphi_s(\mathbf{y})\right]\cdot d\Gamma(\mathbf{y})$$

$$= \int_\Gamma\left[\widetilde{T}_n(\mathbf{y})\cdot\overline{w}^*(\mathbf{y},\mathbf{x}) - M_n(\mathbf{y})\cdot\overline{\varphi}^*_n(\mathbf{y},\mathbf{x})\right]\cdot d\Gamma(\mathbf{y})$$

$$+ \int_\Omega\left(N_x\cdot\frac{\partial^2 w}{\partial x^2} + 2N_{xy}\cdot\frac{\partial^2 w}{\partial x\partial y} + N_y\cdot\frac{\partial^2 w}{\partial y^2}\right)\cdot\overline{w}^*(\mathbf{y},\mathbf{x})\cdot d\Omega(\mathbf{y}).$$

The expression (2.15) denotes shear force for clamped and for simply-supported edges:

$$\widetilde{T}_n(\mathbf{y}) = \begin{cases} V_n(\mathbf{y}), \\ R_n(\mathbf{y}). \end{cases}$$

Because in all the cases (Eqs. (2.3), (2.6) and (2.11), (2.12)) the forces on the real plate: $V_n(\mathbf{y})$ and $T_n(\mathbf{y})$ are multiplied by the same fundamental functions $w^*(\mathbf{y},\mathbf{x})$ and $\overline{w}^*(\mathbf{y},\mathbf{x})$, the force $\widetilde{T}_n(\mathbf{y})$ can be treated as an equivalent shear force $V_n(\mathbf{y})$ on a fragment of the boundary which is located far from the corner. In the case of the free edge we must combine the angle of rotation in the

tangent direction $\varphi_s(\mathbf{y})$ with the fundamental function $M_{ns}^*(\mathbf{y})$. Because the relation between $\varphi_s(\mathbf{y})$ and the deflection is known: $\varphi_s(\mathbf{y}) = \dfrac{\mathrm{d}w(\mathbf{y})}{\mathrm{d}s}$, the angle of rotation $\varphi_s(\mathbf{y})$ can be evaluated using a finite difference scheme of the deflection with two or more adjacent nodal values. In this analysis, the employed finite difference scheme includes the deflections of three adjacent nodes. As a result, the boundary integral Eqs. (2.16) and (2.17) will take the form:

$$(2.18)\quad c(\mathbf{x}){\cdot}w(\mathbf{x})+\int\limits_{\Gamma}\left[T_n^*(\mathbf{y},\mathbf{x}){\cdot}w(\mathbf{y})-M_{ns}^*(\mathbf{y},\mathbf{x}){\cdot}\frac{\mathrm{d}w(\mathbf{y})}{\mathrm{d}s}-M_n^*(\mathbf{y},\mathbf{x}){\cdot}\varphi_n(\mathbf{y})\right]{\cdot}\mathrm{d}\Gamma(\mathbf{y})$$

$$=\int\limits_{\Gamma}\left[\widetilde{T}_n(\mathbf{y})\cdot w^*(\mathbf{y},\mathbf{x})-M_n(\mathbf{y})\cdot\varphi_n^*(\mathbf{y},\mathbf{x})\right]\cdot\mathrm{d}\Gamma(\mathbf{y})$$

$$+\int\limits_{\Omega}\left(N_x\cdot\frac{\partial^2 w}{\partial x^2}+2N_{xy}\cdot\frac{\partial^2 w}{\partial x\partial y}+N_y\cdot\frac{\partial^2 w}{\partial y^2}\right)\cdot w^*(\mathbf{y},\mathbf{x})\cdot\mathrm{d}\Omega(\mathbf{y}),$$

$$(2.19)\quad c(\mathbf{x}){\cdot}\varphi_n(\mathbf{x})+\int\limits_{\Gamma}\left[\overline{T}_n^*(\mathbf{y},\mathbf{x}){\cdot}w(\mathbf{y})-\overline{M}_{ns}^*(\mathbf{y},\mathbf{x}){\cdot}\frac{\mathrm{d}w(\mathbf{y})}{\mathrm{d}s}-\overline{M}_n^*(\mathbf{y},\mathbf{x}){\cdot}\varphi_n(y)\right]{\cdot}\mathrm{d}\Gamma(\mathbf{y})$$

$$=\int\limits_{\Gamma}\left[\widetilde{T}_n(\mathbf{y})\cdot\overline{w}^*(\mathbf{y},\mathbf{x})-M_n(\mathbf{y})\cdot\overline{\varphi}_n^*(\mathbf{y},\mathbf{x})\right]\cdot\mathrm{d}\Gamma(\mathbf{y})$$

$$+\int\limits_{\Omega}\left(N_x\cdot\frac{\partial^2 w}{\partial x^2}+2N_{xy}\cdot\frac{\partial^2 w}{\partial x\partial y}+N_y\cdot\frac{\partial^2 w}{\partial y^2}\right)\cdot\overline{w}^*(\mathbf{y},\mathbf{x})\cdot\mathrm{d}\Omega(\mathbf{y}).$$

3. CONSTRUCTION OF SET OF ALGEBRAIC EQUATIONS

The plate boundary is discretized by elements of the constant type. Three approaches of constructing the boundary integral equations are considered. According to the first one, singular approach, the collocation points are located exactly on the plate boundary (Fig. 1).

According to the second, non-singular approach, the boundary integral equations can be formulated using one collocation point (Fig. 2a) or two collocation points (Fig. 2b) located outside of the plate boundary on the line normal to the plate edge.

It is assumed that a rectangular plate is compressed only by N_x forces. Then, in the boundary integral Eqs. (2.16) and (2.17) takes a stand only the part $N_x \cdot \left(\partial^2 w/\partial x^2\right)$. The unknown variable in internal collocation points is the parameter $\kappa = \partial^2 w/\partial x^2$, the plate curvature in x direction [19, 23]. It is also assumed, that a plate has a regular shape without any holes. According to these
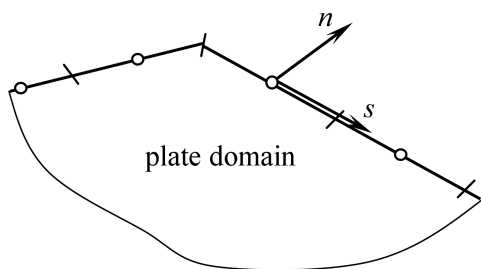
FIG. 1. Collocation point assigned to the boundary element of the constant type.

a)   b)
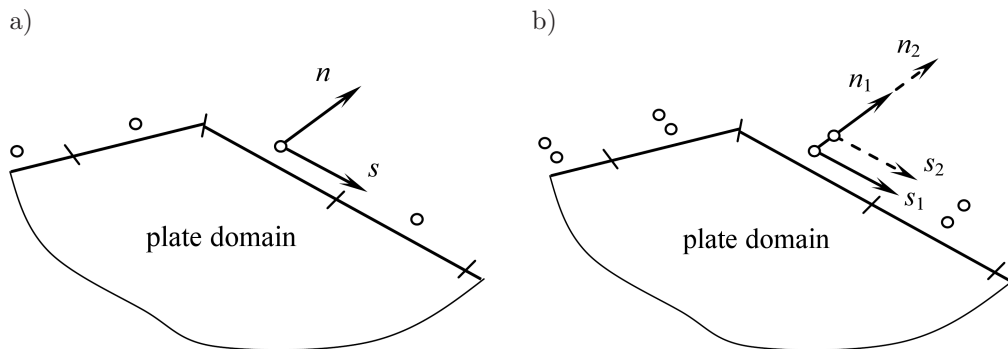
FIG. 2. One collocation point a) and two collocation points b) assigned to the boundary element of the constant type.

assumptions it is possible to accept an arbitrary linear distribution of the normal loading along plate edge perpendicular to the x direction. The plate domain Ω is divided into finite number of sub-domains just to define a plate curvature in selected internal collocation points associated with these sub-domains Ω_m. The normal loading N_x is constant on the length of the single internal sub-domain side which shows Fig. 3.
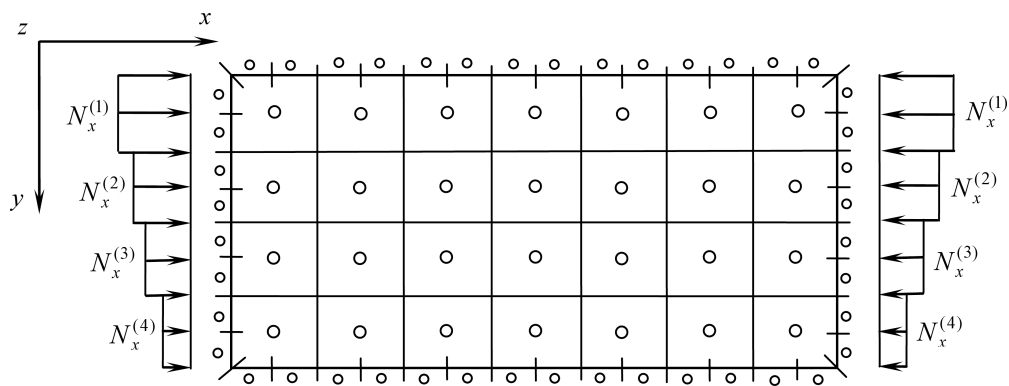
FIG. 3. Distribution of in plane loading.

The set of $N_x^{(i)}$ forces is expressed by the comparative normal loading $N=N_{\mathrm{cr}}$. Hence, the set of algebraic equation can be written in the form [23]:

$$(3.1) \qquad \begin{bmatrix} \mathbf{G_{BB}} & \mathbf{G_{BS}} & -\lambda \cdot \mathbf{G_{B\kappa}} \\ \mathbf{\Delta} & -\mathbf{I} & \mathbf{0} \\ \mathbf{G_{\kappa B}} & \mathbf{G_{\kappa S}} & -\lambda \cdot \mathbf{G_{\kappa\kappa}} + \mathbf{I} \end{bmatrix} \cdot \left\{ \begin{array}{c} \mathbf{B} \\ \varphi_{\mathbf{S}} \\ \boldsymbol{\kappa} \end{array} \right\} = \left\{ \begin{array}{c} \mathbf{0} \\ \mathbf{0} \\ \mathbf{0} \end{array} \right\},$$

where $\lambda = N_{\mathrm{cr}}$ and $\mathbf{G_{BB}}$ and $\mathbf{G_{BS}}$ are the matrices of the dimensions of the dimension $(2N \times 2N)$ and of the dimension $(2N \times S)$ grouping boundary integrals and depend on type of boundary, where N is the number of boundary nodes (or the number of the elements of the constant type) and S is the number of boundary elements along free edge; $\mathbf{G_{B\kappa}}$ is the matrix of the dimension $(2N \times 2N)$ grouping integrals over the internal sub-domains Ω_m; $\mathbf{\Delta}$ is the matrix grouping difference operators connecting angle of rotations in tangent direction with deflections of suitable boundary nodes if a plate has a free edge.

The third matrix equation $(3.1)_3$ in the set of equation (3.1) is obtained by construction the boundary integral equations for internal collocation points associated with internal sub-domains Ω_m. According the typical approach, in this equation, the plate curvature can be derived by double differentiation of boundary integral Eq. (2.16) and by constructing one integral equation with respect to central collocation point "1" belonging to each internal sub-surface. Therefore $\mathbf{G_{\kappa B}}$ is the matrix of the dimension $(M \times 2N)$ grouping the boundary integrals of the second derivatives with respect to the co-ordinate x of the appropriate fundamental functions, where M is the number of the internal collocation points and N is the number of the boundary nodes; $\mathbf{G_{\kappa S}}$ is the matrix of the dimension $(M \times S)$ grouping the boundary integrals of the second derivatives with respect to the co-ordinate x of the appropriate fundamental functions; $\mathbf{G_{\kappa\kappa}}$ is the matrix of the dimension $(M \times M)$ grouping the integrals of the second derivatives with respect to the co-ordinate x over the internal sub-surfaces $\Omega_m \in \Omega$.

In accordance with the simplified approach, the plate curvature can be also establish by addition two internal collocation points ("2" and "3"). Due to this conception it is necessary to construct three integral equation considering three collocation points ("1", "2" and "3") and using Eq. (2.18) in unchanged form. These two approaches are illustrated in Fig. 4.

According the second approach the plate curvature at central point "1" is calculated by constructing difference quotient:

$$(3.2) \qquad \boldsymbol{\kappa} = \boldsymbol{\kappa}_x = \frac{\Delta^2 \mathbf{w}}{\Delta x^2} = \frac{\mathbf{w}_2 - 2 \cdot \mathbf{w}_1 + \mathbf{w}_3}{(\Delta x)^2}.$$
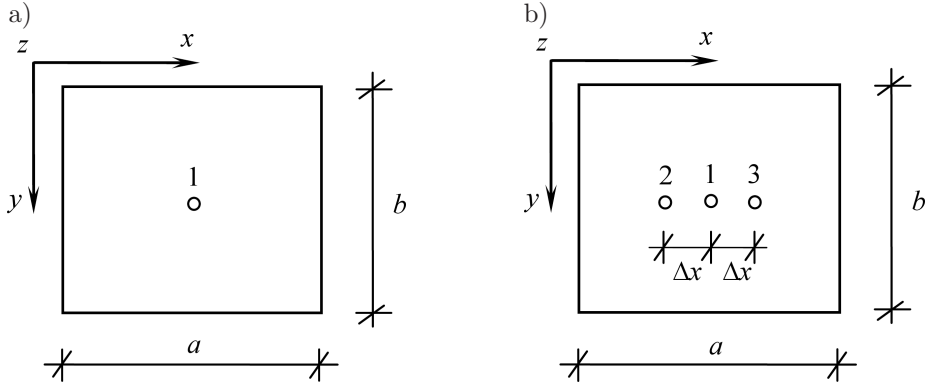
FIG. 4. Definition of the curvature in central collocation point.

Hence elements of the matrices $\mathbf{G_{\kappa B}}$, $\mathbf{G_{\kappa S}}$ and $\mathbf{G_{\kappa\kappa}}$ can be evaluated using three boundary integral equations based only on the boundary integral Eq. (2.18). Elimination of boundary variables $\mathbf{B}$ and $\varphi_{\mathbf{S}}$ from matrix Eq. (3.2) leads to standard eigenvalue problem:

$$(3.3) \qquad \left\{\mathbf{A} - \widetilde{\lambda} \cdot \mathbf{I}\right\} \cdot \boldsymbol{\kappa} = \mathbf{0},$$

where $\widetilde{\lambda} = 1/\lambda$ and

$$(3.4) \qquad \mathbf{A} = \left\{\mathbf{G_{\kappa\kappa}} - (\mathbf{G_{\kappa B}} - \mathbf{G_{\kappa S}} \cdot \boldsymbol{\Delta}) \cdot [\mathbf{G_{BB}} + \mathbf{G_{BS}}]^{-1} \cdot \mathbf{G_{B\kappa}}\right\}.$$

The same problem of plate stability can also be formulated in terms of the Analog Equation Method. The plate bending is expressed by differential Eq. (2.1). It is assumed, that plate is compressed only by N_x forces, the governing equation will take the form

$$(3.5) \qquad D \cdot \nabla^4 w + N_x \cdot \frac{\partial^2 w}{\partial x^2} = 0.$$

The real problem can be replaced by the analogous issue, which is described by the following differential equation

$$(3.6) \qquad \nabla^4 w = b(x, y).$$

In this issue, the boundary conditions are the same as in the real one and $b(x, y)$ is the unknown function of a fictitious loading. The solution of Eq. (3.6) can be expressed using integral representation by two equations:

(3.7) $\ c(\mathbf{x}) \cdot w(\mathbf{x}) + \int_{\Gamma} \left[T_n^*(\mathbf{y},\mathbf{x}) \cdot w(\mathbf{y}) - M_{ns}^*(\mathbf{y},\mathbf{x}) \cdot \dfrac{\mathrm{d}w(\mathbf{y})}{\mathrm{d}s} - M_n^*(\mathbf{y},\mathbf{x}) \cdot \varphi_n(\mathbf{y}) \right] \cdot \mathrm{d}\Gamma(\mathbf{y})$

$$= \int_{\Gamma} \left[\widetilde{T}_n(\mathbf{y}) \cdot w^*(\mathbf{y},\mathbf{x}) - M_n(\mathbf{y}) \cdot \varphi_n^*(\mathbf{y},\mathbf{x}) \right] \cdot \mathrm{d}\Gamma(\mathbf{y})$$

$$+ \int_{\Omega} b(\mathbf{y}) \cdot w^*(\mathbf{y},\mathbf{x}) \cdot \mathrm{d}\Omega(\mathbf{y}),$$

(3.8) $\ c(\mathbf{x}) \cdot \varphi_n(\mathbf{x}) + \int_{\Gamma} \left[\overline{T}_n^*(\mathbf{y},\mathbf{x}) \cdot w(\mathbf{y}) - \overline{M}_{ns}^*(\mathbf{y},\mathbf{x}) \cdot \dfrac{\mathrm{d}w(\mathbf{y})}{\mathrm{d}s} - \overline{M}_n^*(\mathbf{y},\mathbf{x}) \cdot \varphi_n(\mathbf{y}) \right] \cdot \mathrm{d}\Gamma(\mathbf{y})$

$$= \int_{\Gamma} \left[\widetilde{T}_n(\mathbf{y}) \cdot \overline{w}^*(\mathbf{y},\mathbf{x}) - M_n(\mathbf{y}) \cdot \overline{\varphi}_n^*(\mathbf{y},\mathbf{x}) \right] \cdot \mathrm{d}\Gamma(\mathbf{y})$$

$$+ \int_{\Omega} b(\mathbf{y}) \cdot \overline{w}^*(\mathbf{y},\mathbf{x}) \cdot \mathrm{d}\Omega(\mathbf{y}),$$

where the fundamental solution is known and expressed by Eq. (2.5).

The plate domain may be discretized using internal sub-surfaces acting as constant domain elements $\Omega_m \in \Omega$ or linear elements [33, 35]. In each internal collocation point the fictitious loading vector $\mathbf{b}$ is introduced. The boundary-domain integral Eqs. (3.7) and (3.8) allow to specify the boundary conditions on each plate edges and the second derivetives of the plate displacement in each of the internal collocation points. Substitution of Eq. (3.6), Eqs. (3.7) and (3.8) which express the boundary conditions and double-differentiated Eq. (3.7) which describes second derivatives with respect to the x global coordinate into governing Eq. (3.5) leads to the standard eigenvalue problem where the eigen multiplier is equal $\widetilde{\lambda} = 1/N_{\mathrm{cr}}$. If the plate domain is divided into rectangular sub-surfaces of the constant type (each sub-surface is associated with one central collocation point in which the plate curvature is established) the AEM approach becomes special case equivalent to the direct Bèzine technique.

4. Modes of buckling

The elements of the eigenvector $\boldsymbol{\kappa}$ obtained after solution of the standard eigenvalue problem (3.3) present the plate curvatures. The set of the algebraic equation indispensable to calculate the eigenvector $\mathbf{w}$ elements has a form:

$$(4.1) \qquad \begin{bmatrix} \mathbf{G_{BB}} & \mathbf{G_{BS}} & \mathbf{0} \\ \boldsymbol{\Delta} & -\mathbf{I} & \mathbf{0} \\ \mathbf{G_{\kappa B}} & \mathbf{G_{\kappa S}} & \mathbf{I} \end{bmatrix} \cdot \left\{ \begin{array}{c} \mathbf{B} \\ \varphi_{\mathbf{s}} \\ \mathbf{w} \end{array} \right\} = \left\{ \begin{array}{c} \lambda \cdot \mathbf{G_{B\kappa}} \cdot \boldsymbol{\kappa} \\ \mathbf{0} \\ \lambda \cdot \mathbf{G_{\kappa\kappa}} \cdot \boldsymbol{\kappa} \end{array} \right\}.$$

In the set of the Eq. (4.1) the first and second Eqs. $(4.1)_1$ and $(4.1)_2$ are obtained from the first and second equations of (3.1) and the third Eq. $(4.1)_3$ is gotten by construction the boundary integral equations for calculating the plate deflection in internal collocation points. Elimination of the boundary variables $\mathbf{B}$ and $\boldsymbol{\varphi_S}$ from Eq. (4.1) gives the elements of the wanted displacement vector:

$$(4.2) \qquad \mathbf{w} = \lambda \cdot \left[\mathbf{G_{\kappa\kappa}} - (\mathbf{G_{\kappa B}} - \mathbf{G_{\kappa S}} \cdot \mathbf{\Delta}) \cdot [\mathbf{G_{BB}} + \mathbf{G_{BS}}]^{-1} \cdot \mathbf{G_{B\kappa}} \right] \cdot \boldsymbol{\kappa}.$$

5. NUMERICAL EXAMPLES

The initial stability problem of a square and rectangular plates, simply-supported on each edge and a square plate simply- supported on two opposite edges with two remaining free edges is considered. For each of them the critical value of the normal loading is investigated. Each of plate edge is divided by the boundary elements of the constant type with the same length. The set of the internal collocation points is regular. The plate properties are: Young modulus $E = 205$ GPa, Poisson ratio $v = 0.3$. The following notations are assumed:

BEM I – singular formulation of governing boundary-domain integral Eqs. (2.18) and (2.19) with second equation obtained by single differentiation of Eq. (2.18), the vector of curvatures is established by double differentiation of the first governing boundary-domain integral Eq. (2.18);

BEM II – non-singular formulation of governing boundary-domain integral Eqs. (2.18) and (2.19), with second Eq. (2.19) obtained by differentiation of Eq. (2.18), the vector of curvatures is established by double differentiation of the first governing boundary-domain integral Eq. (2.18). The collocation point of single boundary element is located outside, near the plate edge. For one collocation point: $\varepsilon_1 = \widetilde{\delta}_1/d = 0.001$ [23] where $\widetilde{\delta}_1$ is distance of collocation point from the plate edge and d is the boundary element length;

BEM III – non-singular formulation of governing boundary-domain integral Eqs. (2.18) and (2.19), with second Eq. (2.19) obtained for the set of additional collocation points with the same fundamental solution w^*, the vector of curvatures is established by constructing difference quotient (3.2) and fundamental solution w^*. Localization of two collocation points for single boundary element is determined by: $\varepsilon_1 = 0.001$ and $\varepsilon_2 = \widetilde{\delta}_2/d = 0.01$. For three collocation point belonging for each internal sub-domain element: $\varepsilon_\Delta = \Delta x/a = 0.001$.

FEM – regular finite element mesh 0.5 m × 0.5 m and element type of S4R (four node with three degree of freedom per node) of ABAQUS program with reduced integration were assumed into comparative analysis.

The critical force N_{cr} is expressed using non-dimensional term:

(5.1)
$$\widetilde{N}_{\mathrm{cr}} = \frac{N_{\mathrm{cr}}}{D} \cdot l_x \cdot l_y.$$

5.1. A simply-supported rectangular plate under uniformly constant normal loading

Static and loading scheme is shown in the Fig. 5.
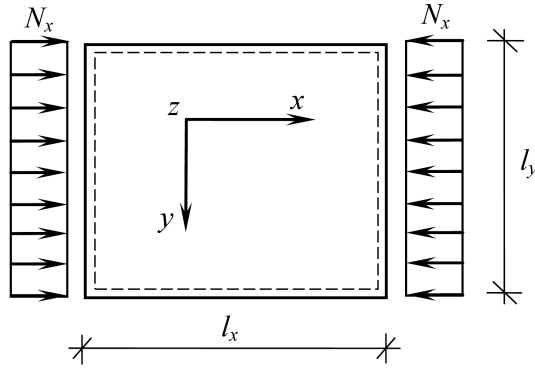
FIG. 5. A simply-supported rectangular plate under uniformly constant normal loading.

Two plates are considered: a) square and b) rectangular. In case a) the plate boundary was discretized using 256 number of boundary elements. The number of internal sub-surfaces used to describe the plate curvature is equal: 256. The plate geometry is defined as: $l_x = l_y = l = 2.0$ m. In case b) the plate boundary was discretized using 128 number of boundary elements. The number of internal sub-surfaces used to describe the plate curvature is equal: 512. The plate geometry is defined as: $l_x = 0.5 \cdot l_y = 2.0$ m. In both cases the following the plate thickness is equal $h = 0.05$ m. Each plate edge is divided into number of 64 in case a) and 32 in case b) boundary elements of the same length. The set of internal square sub-domains is reagular. The results of calculation are presented in Tables 1–3. The influence of localization of internal collocation points on critical force values for square plate a) using BEM III approach is presented in Table 2.

Table 1. Critical force values: $l_x/l_y = 1.0$.

$\widetilde{N}_{\mathrm{cr}}$	Analytical solution [40, 41]	BEM I solution	BEM II solution	BEM III solution
1	39.4784	39.6198	39.6228	39.6350
2	61.6850	62.1887	62.1916	62.1996
3	109.6623	111.3933	111.3962	111.4057

Table 2. Critical force values: $l_x/l_y = 0.5$.

$\widetilde{N}_{cr}$	Analytical solution [40, 41]	BEM I solution	BEM II solution	BEM III solution
1	30.8425	30.9227	30.9230	30.9253

Table 3. Critical force values: $l_x/l_y = 1.0$. Solution BEM III for different value of $\varepsilon_\Delta = \Delta x/a$.

$\widetilde{N}_{cr}$	$\varepsilon_\Delta = \Delta x/a$				
	0.0001	0.001	0.01	0.1	0.2
1	39.6350	39.6350	39.6351	39.6362	39.6398
2	62.1993	62.1996	62.1996	62.2073	62.2311
3	111.4057	111.4057	111.4057	111.4385	111.5362
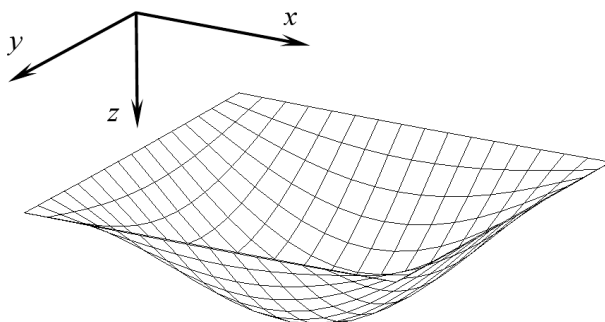
FIG. 6. The first buckling mode, $l_x/l_y = 1.0$.
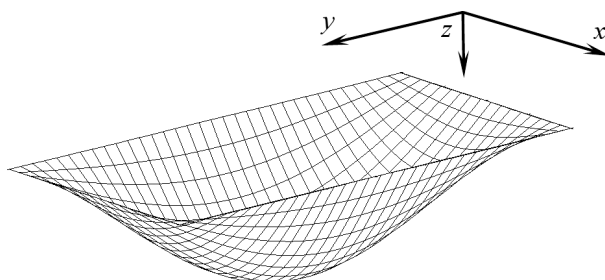
FIG. 7. The first buckling mode, $l_x/l_y = 0.5$.

5.2. A simply-supported rectangular plate under uniformly linear normal loading

Static and loading scheme is shown in the Fig. 8.

Two plates are considered: a) square and b) rectangular. In case a) the plate boundary was discretized using 256 number of boundary elements (64 elements
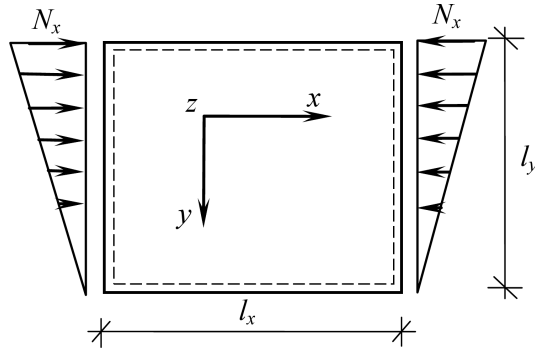
FIG. 8. A simply-supported rectangular plate under uniformly linear normal loading.

on each edge). The number of internal sub-surfaces used to describe the plate curvature is equal: 256. The plate geometry is defined as: $l_x = l_y = l = 2.0$ m. In case b) the plate boundary was discretized using 128 number of boundary elements (32 elements on each edge). The number of internal sub-surfaces used to describe the plate curvature is equal: 384. The plate geometry is defined as: $l_x = 1.5 \cdot l_y = 3.0$ m. In both cases the plate properties were assumed identically as in Example 5.1. The results of calculation are presented in Tables 4–6.

Table 4. Critical force values $l_x/l_y = 1.0$.

$\widetilde{N}_{\mathrm{cr}}$	Analytical solution [41]	BEM I solution	BEM II solution	BEM III solution
1	76.9829	77.3858	77.3918	77.4153
2	–	115.7346	115.7401	115.7566
3	–	194.3706	194.3797	194.4041

Table 5. Critical force values: $l_x/l_y = 1.0$. Solution BEM III for different value of $\varepsilon_\Delta = \Delta x/a$.

$\widetilde{N}_{\mathrm{cr}}$	$\varepsilon_\Delta = \Delta x/a$				
	0.0001	0.001	0.01	0.1	0.2
1	77.4153	77.4153	77.4153	77.4175	77.4245
2	115.7566	115.7566	115.7566	115.7707	115.8148
3	194.4038	194.4041	194.4043	194.4599	194.6296

Table 6. Critical force values $l_x/l_y = 1.5$.

$\widetilde{N}_{\mathrm{cr}}$	Analytical solution [41]	BEM I solution	BEM II solution	BEM III solution
1	124.3570	124.5210	124.5241	124.5283

The influence of localization of internal collocation points on critical force values for square plate a) using BEM III approach is presented in Table 5.
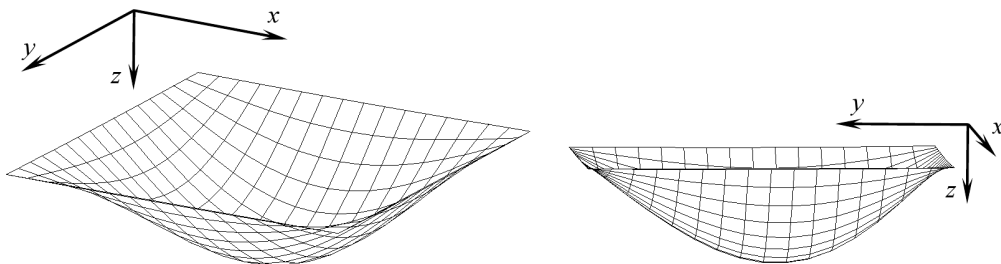
FIG. 9. The first buckling mode, $l_x/l_y = 1.0$.
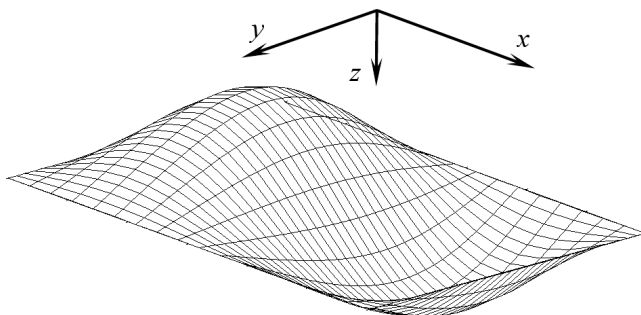
FIG. 10. The first buckling mode, $l_x/l_y = 1.5$.

5.3. A simply-supported rectangular plate under uniformly linear normal loadings

Static and loading scheme is shown in the Fig. 11.
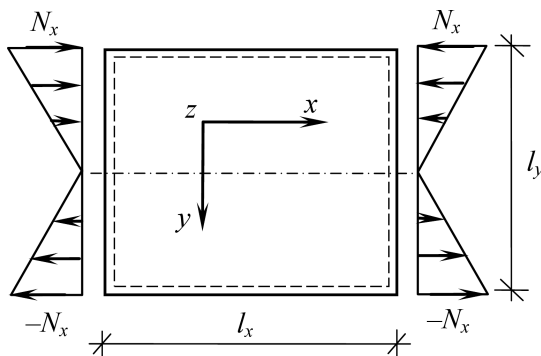
FIG. 11. A simply-supported rectangular plate under uniformly linear normal loadings.

Two plates are considered: a) square and b) rectangular. In both cases the plate geometry, properties and discretization were assumed identically as in Example 5.2. The results of calculation are presented in Tables 7–9. Number of real critical force value is given in the first column. Number of computational value is indicated beside by roman numerals. The influence of localization of internal collocation points on critical force values for square plate a) using BEM III approach is presented in Table 8.

Table 7. Critical force values, $l_x/l_y = 1.0$.

$\widetilde{N}_{\text{cr}}$	Analytical solution [41]	BEM I solution	BEM II solution	BEM III solution
1 (I)	252.6619	254.8014	254.8211	254.8753
2 (III)	–	269.1932	269.2128	269.2808
3 (V)	–	340.3840	340.4153	340.4976

Table 8. Critical force values: $l_x/l_y = 1.0$. Solution BEM III for different value of $\varepsilon_\Delta = \Delta x/a$.

$\widetilde{N}_{\text{cr}}$	$\varepsilon_\Delta = \Delta x/a$				
	0.0001	0.001	0.01	0.1	0.2
1 (I)	254.8753	254.8753	254.8753	254.9058	254.9984
2 (III)	269.2813	269.2808	269.2808	269.2872	269.3072
3 (V)	340.4969	340.4976	340.4983	340.5935	340.8843

Table 9. Critical force values, $l_x/l_y = 1.5$.

$\widetilde{N}_{\text{cr}}$	Analytical solution [41]	BEM I solution	BEM II solution	BEM III solution
1 (I)	356.7861	359.7330	359.7432	359.7538
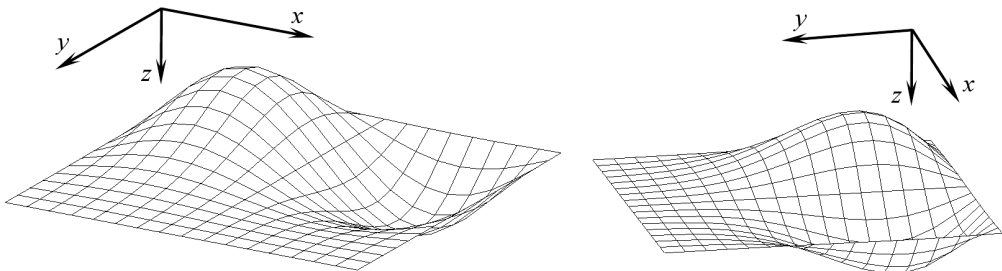
FIG. 12. The first buckling mode, $l_x/l_y = 1.0$.
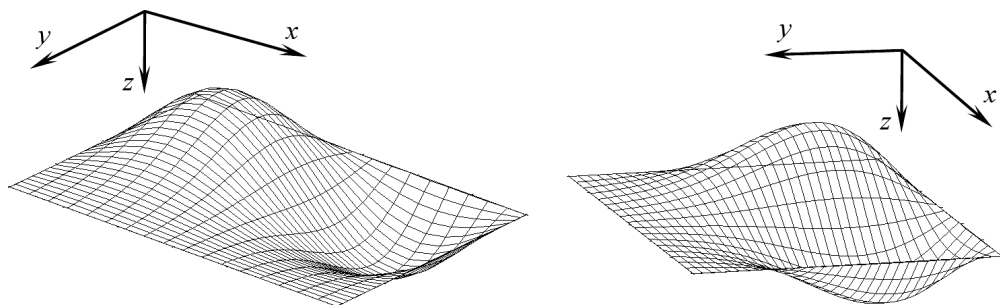
FIG. 13. The first buckling mode, $l_x/l_y = 1.5$.

5.4. A rectangular plate simply-supported on two opposite edges with two remaining edges free under uniformly constant normal loading

Static and loading scheme is shown in the Fig. 14.
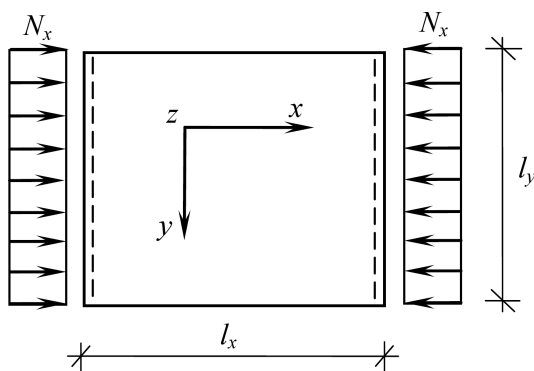
FIG. 14. A rectangular plate simply-supported on two opposite edges with two remaining free edges under uniformly constant normal loading.

Two plates are considered: a) square and b) rectangular. In both cases the plate geometry, properties and discretization were assumed identically as in Example 5.2. The results of calculation are presented in Tables 10–12. The influence

Table 10. Critical force values, $l_x/l_y = 1.0$.

$\widetilde{N}_{\mathrm{cr}}$	FEM solution	BEM II solution	BEM III solution
1	9.4603	9.8082	9.5546
2	26.5097	25.7486	25.4393
3	39.4389	38.2109	38.1065

Table 11. Critical force values: $l_x/l_y = 1.0$. Solution BEM III for different value of $\varepsilon_\Delta = \Delta x/a$.

$\widetilde{N}_{\mathrm{cr}}$	$\varepsilon_\Delta = \Delta x/a$				
	0.0001	0.001	0.01	0.1	0.2
1	9.5546	9.5546	9.5527	9.5527	9.5477
2	25.4394	25.4393	25.4266	25.4266	25.3927
3	38.1064	38.1065	38.1014	38.1015	38.0892

Table 12. Critical force values, $l_x/l_y = 1.5$.

$\widetilde{N}_{\mathrm{cr}}$	FEM solution	BEM II solution	BEM III solution
1	6.1887	6.4995	6.4041

of localization of internal collocation points on critical force values for square plate a) using BEM III approach is presented in Table 11.
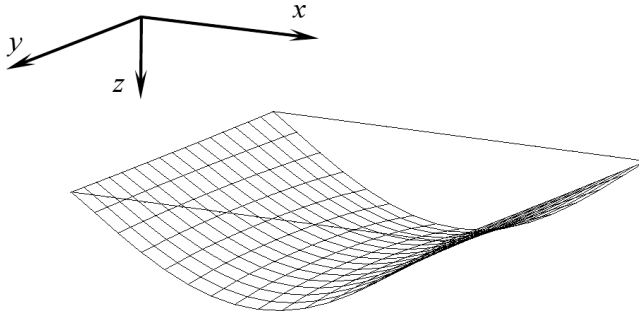
FIG. 15. The first buckling mode, $l_x/l_y = 1.0$.
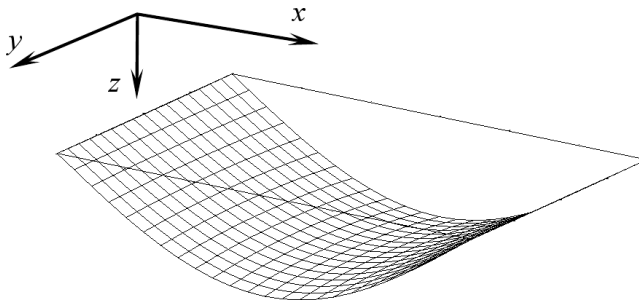
FIG. 16. The first buckling mode, $l_x/l_y = 1.5$.

5.5. A rectangular plate simply-supported on two opposite edges with two remaining free edges under uniformly linear normal loading

Static and loading scheme is shown in the Fig. 17.
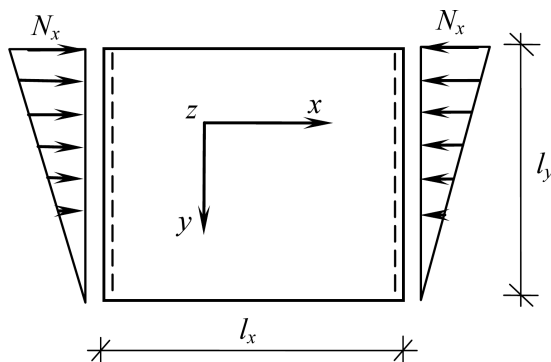
FIG. 17. A rectangular plate simply-supported on two opposite edges with two remaining free edges under uniformly linear normal loading.

Two plates are considered: a) square and b) rectangular. In both cases the plate geometry, properties and discretization were assumed identically as in Example 5.2. The results of calculation are presented in Tables 13–15. The influence of localization of internal collocation points on critical force values for square plate a) using BEM III approach is presented in Table 14.

Table 13. Critical force values, $l_x/l_y = 1.0$.

$\widetilde{N}_{\mathrm{cr}}$	FEM solution	BEM II solution	BEM III solution
1	16.7221	16.3165	16.3162
2	56.6365	54.5680	54.2951
3	83.2673	81.7806	81.0573

Table 14. Critical force values: $l_x/l_y = 1.0$. Solution BEM III for different value of $\varepsilon_\Delta = \Delta x/a$.

$\widetilde{N}_{\mathrm{cr}}$	$\varepsilon_\Delta = \Delta x/a$				
	0.0001	0.001	0.01	0.1	0.2
1	16.3162	16.3162	16.3162	16.3112	16.2983
2	54.2953	54.2951	54.2951	54.2766	54.2288
3	81.0572	81.0573	81.0569	81.0345	80.9748

Table 15. Critical force values, $l_x/l_y = 1.5$.

$\widetilde{N}_{\mathrm{cr}}$	FEM solution	BEM II solution	BEM III solution
1	11.4891	11.9982	11.8209
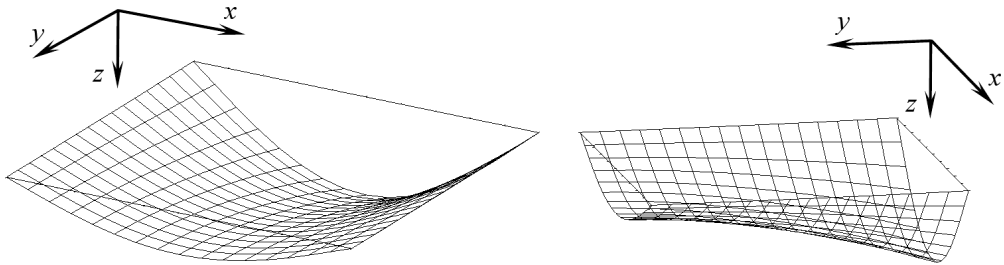
FIG. 18. The first buckling mode, $l_x/l_y = 1.0$.
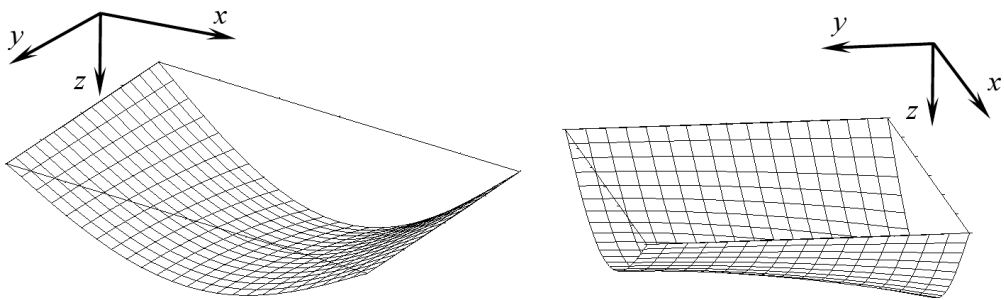
FIG. 19. The first buckling mode, $l_x/l_y = 1.5$.

5.6. A rectangular plate simply-supported on two opposite edges with two remaining free edges under uniformly linear normal loadings

Static and loading scheme is shown in the Fig. 20.
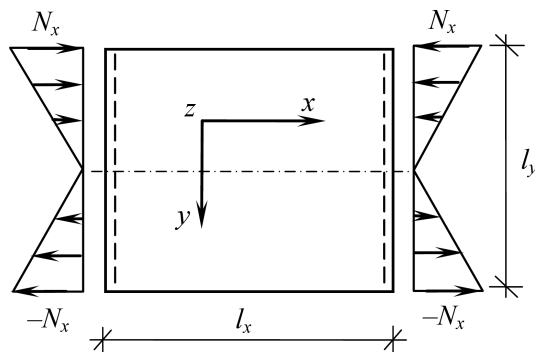
FIG. 20. A rectangular plate simply-supported on two opposite edges with two remaining free edges under uniformly linear normal loadings.

Two plates are considered: a) square and b) rectangular. In both cases the plate geometry, properties and discretization were assumed identically as in Example 5.2. The results of calculation are presented in Tables 16–18. Number of real critical force value is given in the first column. Number of computational value is indicated beside by roman numerals. The influence of localization of internal collocation points on critical force values for square plate a) using BEM III approach is presented in Table 17.

Table 16. Critical force values, $l_x/l_y = 1.0$.

$\widetilde{N}_{\mathrm{cr}}$	FEM solution	BEM II solution	BEM III solution
1 (I)	25.9506	25.9804	25.4095
2 (III)	71.5806	68.6190	68.1714
3 (V)	150.0035	134.4278	133.1770

Table 17. Critical force values: $l_x/l_y = 1.0$. Solution BEM III for different value of $\varepsilon_\Delta = \Delta x/a$.

$\widetilde{N}_{\mathrm{cr}}$	$\varepsilon_\Delta = \Delta x/a$				
	0.0001	0.001	0.01	0.1	0.2
1 (I)	25.4094	25.4095	25.4093	25.3956	25.3586
2 (III)	68.1714	68.1714	68.1709	68.1346	68.0386
3 (V)	133.1770	133.1770	133.1759	133.1156	132.9640

Table 18. Critical force values, $l_x/l_y = 1.5$.

$\widetilde{N}_{\mathrm{cr}}$	FEM solution	BEM II solution	BEM III solution
1 (I)	23.5430	23.9012	23.5336
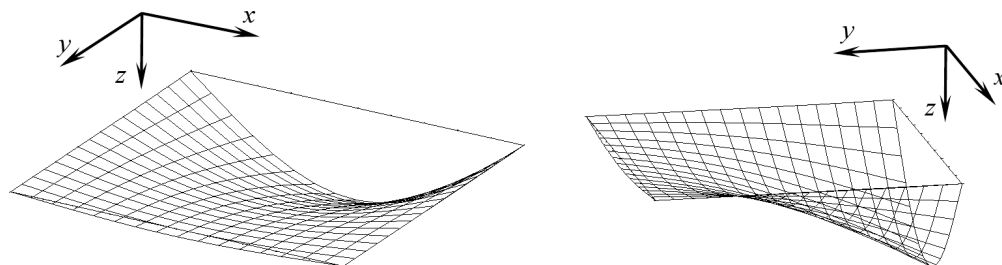
FIG. 21. The first buckling mode, $l_x/l_y = 1.0$.
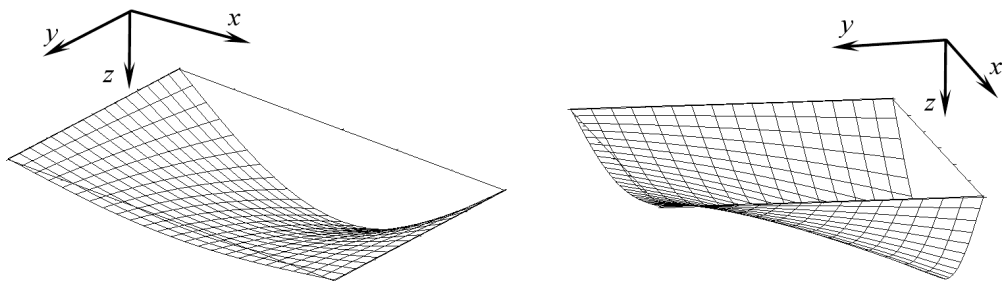
FIG. 22. The first buckling mode, $l_x/l_y = 1.5$.

6. CONCLUSIONS

An initial stability of thin plates using the boundary element method is presented. This problem was solved with the modified approach, in which the boundary conditions are defined so that there is no need to introduce equivalent boundary quantities dictated by the boundary value problem for the biharmonic differential equation. The collocation version of boundary element method with singular and non-singular calculations of integrals were employed and the constant type of the boundary element is introduced. The Bèzine technique was used to establish the vector of curvatures inside a plate domain which was divided into rectangular sub-surfaces. A plate can be subjected in plane by loading which distribution can be arbitrary, constant along selected edge of the single sub-domain element. The high number of boundary elements and internal sub-surfaces is not required to obtain sufficient accuracy. The loaded plate edge must be supported. This condition is required in proposed formulation of buckling analysis.

In case of normal conservative loading along the plate free edge, the boundary integral equation must be expanded by additional part:

$$\int\limits_{\Gamma} -N_x \cdot \frac{\partial w_b}{\partial x} \cdot w^*(\mathbf{y}, \mathbf{x}) \cdot \mathrm{d}\Gamma(\mathbf{y}).$$

Then, construction of set of algebraic equation in matrix notation and formulation of the standard eigenvalue problem are much more complicated. To solve this problem, the first and second derivatives of deflection inside the plate area $(\partial^2 w/\partial x^2)$ and at the boundary $(\partial w_b/\partial x)$ can be establish and calculated for example approximately by constructing a differential expression using deflections of suitable neighbouring internal collocation points belonging to different internal sub-domains and collocation points located at the plate free edge.

The boundary element results obtained for presented conception of thin plate bending issue demonstrate the sufficient effectiveness and efficiency of the pro-

posed approach which can be useful in engineering analysis of the buckling problem.

Acknowledgment

References

1. Burczyński T., *The Boundary Element Method in Mechanics* (in Polish), Technical-Scientific Publishing house, Warszawa, 1995.

2. Altiero N.J., Sikarskie D.L., *A boundary integral method applied to plates of arbitrary plane form*, Computers and Structures, **9**, 163–168, 1978.

3. Bèzine G., Gamby D.A., *A new integral equations formulation for plate bending problems*, Advances in Boundary Element Method, Pentech Press, London, 1978.

4. Stern M., *A general boundary integral formulation for the numerical solution of plate bending problems*, International Journal od Solids and Structures, **15**, 769–782, 1978.

5. Hartmann F., Zotemantel R., *The direct boundary element method in plate bending*, International Journal of Numerical Method in Engineering, **23**, 2049–2069, 1986.

6. Debbih M., *Boundary element method versus finite element method for the stress analysis of plates in bending*, MSc Thesis, Cranfield Institute of Technology, Bedford, 1987.

7. Debbih M., *Boundary element stress analysis of thin and thick plates*, PhD Thesis, Cranfield Institute of Technology, Bedford, 1989.

8. Abdel-Akher A., Hartley G.A., *Evaluation of boundary integrals for plate bending*, International Journal of Numerical Method in Engineering, **28**, 75–93, 1989.

9. Hartley G.A., *Development of plate bending elements for frame analysis*, Engineering Analysis with Boundary Element, **17**, 2, 93–104, 1997.

10. Beskos D.E., *Dynamic analysis of plates by boundary elements*, Applied Mechanics Review, **7**, 26, 213–236, 1999.

11. Wen P.H., Aliabadi M.H., Young A., *A boundary element method for dynamic plate bending problems*, International Journal od Solids and Structures, **37**, 5177–5188, 2000.

12. Wrobel L.C., Aliabadi M.H., *The Boundary Element Methods in Engineering*, McGraw-Hill College, ISBN 0–07–707769–5, 2002.

13. Katsikadelis J.T., *A boundary element solution to the vibration problem of plates*, Journal of Sound and Vibration, **141**, 2, 313–322, 1990.

14. Katsikadelis J.T., *A boundary element solution to the vibration problem of plates*, International Journal of Solids and Structures, **27**, 15, 1867–1878, 1991.

15. Katsikadelis J.T., Yotis A.J., *A New boundary element solution of thick plates modelled by Reissner's theory*, Engineering Analysis with Boundary Elements, **12**, 1, 65–74, 1999.

16. KATSIKADELIS J.T., SAPOUNTZAKIS E.J., ZORBA E.G., *A BEM Approach to Static and Dynamic Analysis with Internal Supports*, Computational Mechanics, **7**, 1, 31–40, 1990.

17. KATSIKADELIS J.T., KANDILAS C.B., *A flexibility matrix solution of the vibration problem of plates based on the Boundary Element Method*, Acta Mechanica, **83**, 1–2, 51–60, 1990.

18. KATSIKADELIS J.T., SAPOUNTZAKIS E.J., *A BEM Solution to dynamic analysis of plates with variable thickness*, Computational Mechanics, **7**, 5–6, 369–379, 1991.

19. SHI G., *Flexural vibration and buckling analysis of orthotropic plates by the boundary element method*, Int. J. Solids Structures, **12**, 26, 1351–1370, 1990.

20. GUMINIAK M., OKUPNIAK B., SYGULSKI R., *Analysis of plate bending by boundary element method*, [in:] Proceedings of European Conference on Computational Mechanics ECCM-2001, Abstarcts, 1, 176–177, Z. Waszczyszyn, J. Pamin [Eds.], Krakow 2001.

21. GUMINIAK M., *Analysis of thin plates by the boundary element method using modified formulation of boundary condition* [in Polish], Doctoral dissertation, Poznan University of Technology, Faculty of Civil Engineering, Architecture and Environmental Engineering, 2004.

22. GUMINIAK M., SYGULSKI R., *Vibrations of system of plates immersed in fluid by BEM*, Proceedings of IIIrd European Conference on Computational Mechanics, Solids, Structures and Coupled Problems in Engineering ECCM-2006, pp. 211, C.A. Mota Soares, J.A.C. Rodrigues, J.A.C. Ambrósio, C.A.B. Pina, C.M. Mota Soares, E.B.R. Pereira and J. Folgado [Eds.], CD enclosed, June 5–9, 2006, Lisbon, Portugal.

23. GUMINIAK M., SYGULSKI R., *Initial stability of Kirchhoff plates by the boundary element method using a modified formulation of a boundary condition*, Foundations of Civil and Environmental Engineering, **7**, 171–186, 2006.

24. GUMINIAK M., SYGULSKI R., *The analysis of internally supported thin plates by the Boundary Element Method. Part 1 – Static analysis*, Foundation of Civil and Environmental Engineering, **9**, 17–41, 2007.

25. GUMINIAK M., SYGULSKI R., *The analysis of internally supported thin plates by the Boundary Element Method. Part 2 – Free vibration analysis*, Foundation of Civil and Environmental Engineering, **9**, 43–74, 2007.

26. MYŚLECKI K., *Approximate fundamental solutions of equilibrium equations for thin plates on an elastic foundation*, Archives of Civil and Mechanical Engineering, **1**, 4, 2004.

27. MYŚLECKI K., *Metoda elementów brzegowych w statyce dźwigarów powierzchniowych* [in Polish], Oficyna Wydawnicza Politechniki Wrocławskiej, Wrocław 2004.

28. MYŚLECKI K., OLEŃKIEWICZ J., *Analiza częstości drgań własnych płyty cienkiej metodą elementów brzegowych* [in Polish], Problemy naukowo-badawcze budownictwa, Wydawnictwo Politechniki Białostockiej, Białystok, **2**, 511–516, 2007.

29. OLEŃKIEWICZ J., *Analiza drgań wybranych dźwigarów powierzchniowych metodą elementów brzegowych*, Rozprawa doktorska, Politechnika Wrocławska, Instytut Inżynierii Lądowej, 2011.

30. LITEWKA B., *Analysis of Reissner plates by the boundary element method with interaction with liquid, Doctoral dissertation* [in Polish], Poznan University of Technology, Faculty of Civil and Environmental Engineering, 2007.

31. LITEWKA B., SYGULSKI R., *Application of the fundamental solutions by Ganowicz in a static analysis of Reissner's plates by the boundary element method*, Engineering Analysis with Boundary Elements, **34**, 1072–1081, 2010.

32. GANOWICZ R., *Selected problems of theory of Reissner and three layer plates* [in Polish], Theoretical and Applied Mechanics, **3–4**, 55–95, 1966.

33. KATSIKADELIS J.T., ΣYNOPIAKA ΣTOIXEIA, Tομος II: Aνλυση Πλακν, 2^{η} Eκδοση, EMΠ 2010 (Katsikadelis J.T., Boundary Elements: Vol. II, Analysis of Plates, Second Edition, NTUA, Athens, 260, 2010).

34. KATSIKADELIS J.T., *The analog equation method – A powerful BEM-based solution technique for solving linear and nonlinear engineering problems*, [in:] Boundary Element Method XVI: 167–182, Brebbia C.A. [Ed.], Computational Mechanics Publications, Southampton, 1994.

35. NERANTZAKI M.S., KATSIKADELIS J.T., *Buckling of plates with variable thickness – An Analog Equation Solution*, Engineering Analysis with Boundary Elements, **18**, 2, 149–154, 1996.

36. CHINNABOON B., CHUCHEEPSAKUL S., KATSIKADELIS J.T., *A BEM–based Meshless Method for Buckling Analysis of Elastic Plates with Various Boundary Conditions*, International Journal of Structural Stability and Dynamics, **7**, 1, 81–89, 2007.

37. BABOUSKOS N., KATSIKADELIS J.T., *Flutter instability of damped plates under combined conservative and nonconservative loads*, Archive of Applied Mechanics, **79**, 541–556, 2009.

38. KATSIKADELIS J.T., BABOUSKOS N.G., *Nonlinear flutter instability of thin damped plates: A solution by the analog equation method*, Journal of Mechanics of Materials and structures, **4**, 7–8, 1395–1414, 2009.

39. GUMINIAK M., LITEWKA B., *Selected problems of thin and thick plates theory in terms of BEM*, Foundations of Civil and Environmental Engineering, **15**, 41–90, 2012.

40. GIRKMANN K., *Plane Girders* [in Polish], Warszawa, Arkady, 1957.

41. TIMOSHENKO S., WOINOWSKY-KRIEGER S., *Theory of plates and shells*, Warszawa, Arkady, 1962.

Failure Assessment of Steel-Concrete Composite Column Under Blast Loading

Marcin P. BUDZIAK, Tomasz GARBOWSKI

Poznan University of Technology
Institute of Structural Engineering
Piotrowo 5, 60-965 Poznań, Poland
e-mail: tomasz.garbowski@put.poznan.pl

Composite column as a key structural member can be subjected to a blast load as a result of an accident or a terrorist threat. In this paper, a method for assessing the blast resistance of a composite concrete-filled column is proposed. Moreover, different methods of enhancing composite member resistance to explosions are investigated. The blast situation is modeled in the FEM software using the CONWEP tool. This empirical formulation is relatively cheap from the computational point of view, as well as precise enough, hence it was chosen for this work purposes. Material models are based on well known elasto-plastic with linear hardening concepts. Important phenomenons are also taken into account, such as: contact formulation between the column components, strain rate dependence, damage initiation and evolution. Simulations are conducted for the most common type of explosion – surface blast. Its main feature is the effect of reflection of the ground surface and hence, amplification of the blast wave after the charge ignition. Results are presented in terms of minimum TNT mass equivalent required for a column member failure.

Key words: composite column, blast loading, failure assessment.

1. Introduction

Designing a building is a process where many goals such as functionality, aesthetic appearance, durability, bearing capacity have to be achieved. However, the most important thing is to provide safety to the users. Recent years show, that structural engineers have to bring more attention to accidental loading, from which explosions seem to be the most dangerous, as they can significantly damage the structure or even cause its total failure. The most fateful cases such as World Trade Center collapse on 11th September 2001 [21] are very well described explaining specific causes and effects. Hence, possible acts of terrorism have to be taken into consideration all over the world, at the earliest buildings' life phase during the design procedure. Also industrial buildings, where

explosion risk exists due to explosive materials production or storage, should be investigated for resistance to such events. In the literature a lot of examples may be found to prove the necessity of assessment the structural response of a building in a blast situation.

Apart from the structure strength some phenomena should not be neglected. First, the difference has to be studied between detonation of charge in the air and on the ground surface. The second situation is much more common and unfortunately much more destructive. What is more complex, the enhancement of damage depends on the type of ground. The more energy is dissipated in producing a crater and groundshock, the less damage to the structure may be observed. Another important issue is the "tunneling" effect in narrow city streets [22]. Low distance between buildings results in confinement of the blast wave. It is reflected and refracted repeatedly of the facades' surfaces, hence the damages occur higher than might be expected in open air conditions. Either the glazing type of facades has its impact on the blast wave [23]. The shockwave front penetrates through the openings and people are subjected to sudden pressures and shattered particles of windows, doors, etc. If the external walls are not able to resist the pressure peak they are fractured and moved by the wave following the shock front causing much more serious damages.

Since aforementioned external conditions would distort this investigation results, a separated fragment of the structure will be studied. A column member can be fairly considered as a critical point of the building, hence it was chosen as a subject of the simulations. Empirical tests of explosions are very expensive and time consuming, what results in quite low accessibility of such experiments in civil engineering field [24]. Fortunately, it is feasible, to conduct numerical simulations at relatively low cost of both an explosion taking place in given space and time, as well as the structure response to such action. Moreover, there exist a need to provide to structural designers a reliable tools for assessing structure resistance in terms of blast situation.

Any realistic simulation of a blast effect on the structure requires suitable constitutive models of structural materials as steel, concrete, glass, etc. Material models characterized by a standard and/or new testing methods in quasi-static conditions (see e.g. [8, 9]) are applicable only in specific range of strain rates. Popular material models of concrete, e.g. Drucker-Prager [7], Lubliner [19], Lee-Fenves [18] can be successfully used in quasi static elasto-plastic-damage analysis (see e.g. [10, 20]), however, they require slight modifications if one wants to use them in dynamic analyzes. The same concerns traditional material model of steel, e.g. Huber-Mises-Hencky, Johnson-Cook [26] or Gurson [13]. Once constitutive models are enhanced by additional features as damage evolution or fracturing in high strain rates the sophisticated test has to be performed (e.g. Split Hopkinson Pressure Bar test also known as Kolsky bar test

[11, 25]) for material characterization and hence more parameters need to be involved in computations. These new parameters, ensuring they are properly identified, lead to realistic computer simulations of the structure subjected to impact loads.

In this work authors employed available in literature simplified modeling of blast phenomenon as well as traditional constitutive models of structural elements enhanced by damage definition and strain rate dependency. The main goal is to predict the failure mechanism and provide possible reinforcing methods of critical elements of a public buildings structure.

2. Blast model

By definition, an explosion is a rapid release of big amount of energy. It is accompanied by a blast wave which is heat and pressure wave propagation in space. The latter is subject to many research and investigation as its outcome causes the most serious consequences to structures. The blast produces a shock wave composed of a high-intensity shock front which expands outward from the surface of the explosive into the surrounding air. Pressure immediately behind the detonation front is in range from 19,000 MPa to 33,800 MPa (Unified Facilities Criteria 3-340-02, December 2008). Only about one-third of the total chemical energy available in most high explosives is released in the detonation process. The remaining two-thirds are released more slowly in explosions in air as the detonation products mix with air and burn. This afterburning process has only a slight effect on blast wave properties, because it is much slower than detonation.

Throughout the pressure-time profile (Fig. 1), two main phases can be observed – portion above ambient is called positive phase duration, whereas that below ambient is called negative phase duration. The negative phase is of a longer duration and a lower intensity than the positive duration. The shock wave overpressure curve is important from the standpoint of civil engineer as it a basis for determination of dynamic pressure. The dynamic pressure determines the value of loading that is subjecting the structure. Generally blast loading on a structure caused by a high-explosive detonation is dependent upon several factors:

- the magnitude of the explosion,
- the location of the explosion relative to the structure of interest (confined or unconfined),
- the geometrical configuration of the structure,
- the structure orientation with respect to the explosion and the ground surface (above, flush with, or below the ground).
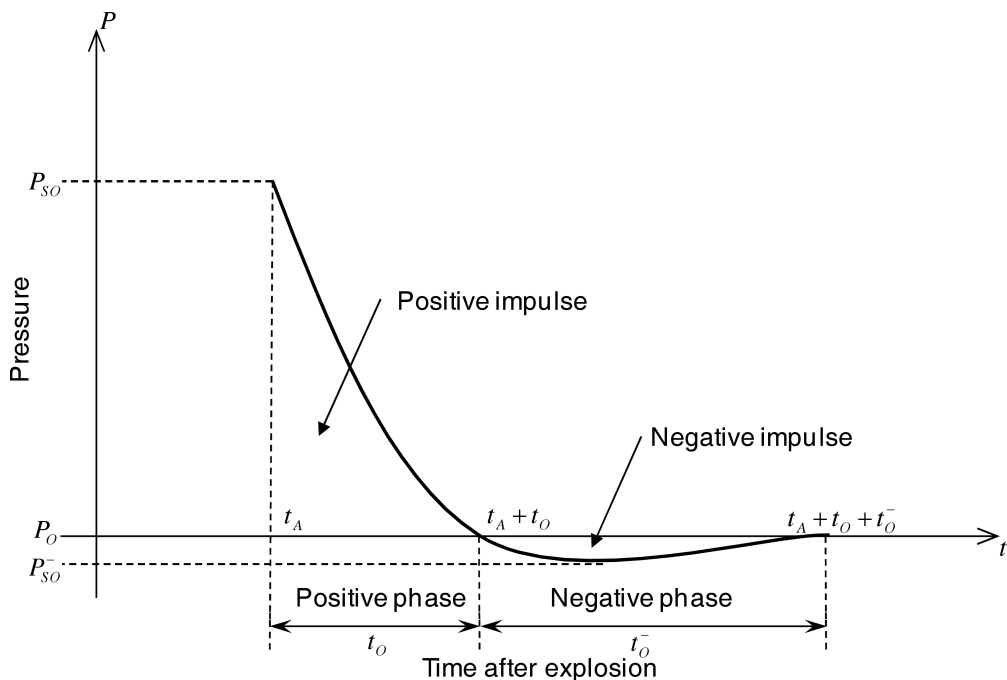
Fig. 1. Relation between time and shock wave pressure.

2.1. Blast-loading classification

Two blast-loading categories can be distinguished. The division bases on the confinement of the explosive charge, and so there are unconfined and confined explosions. For this purposes only two most representative and commonly encountered in practice types of unconfined explosions are presented.

First is called Air Blast and applies to events, where the charge is detonated in free air, enabling unconstrained blast wave propagation.

The second type is known as Surface Blast, which refers to the situation where source of the shock wave is located close to, or on the ground surface. The initial wave of the explosion is reflected and reinforced by the ground surface to produce a reflected wave. Unlike the air burst, the reflected wave merges with the incident wave at the point of detonation to form a single wave, similar in nature to the Mach wave of the air burst but essentially hemispherical in shape.

2.2. Numerical model of blast event

The most considered effect of an explosion is blast overpressure wave. Various methods of estimating the blast peak overpressure based on empirical formulas

were collected in literature [3, 23], however all they base on a scaled distance, which is denoted as:

$$(2.1) \qquad Z = \frac{R}{W^{1/3}},$$

where R is distance to the charge and W is mass of the charge given in kg of TNT.

Numerical methods of analyzing explosion problems and blast-loading modeling can be divided into two stages. First, modeling of the shock wave. Second, formulation of the interaction with a structure subjected to such load. Blast wave modeling requires the determination of the charge weight given in TNT-equivalent and charge localization coordinates. Also type of the explosion has to be selected as the air or surface blast. Output data returns a pressure in given space point, occurring at a given time.

One of the most commonly used numerical tool for blast modeling is ConWep. It is mathematical model based on empirical data of experimental detonations of explosives of masses from less than 1 kg to over 400 000 kg [17]. This data was then scaled using Hopkinson and Sachs scaling laws to standard atmospheric sea level conditions. Formulas prepared by Kingery and Bulmash [17] allow estimating shock wave parameters basing on TNT only. For other explosives TNT-equivalent has to be used accordingly to its type. Once the parameters of peak overpressure, time of arrival and time of duration are determined, the value of the pressure in time is given by the modified Friedlander's Equation proposed in [3]:

$$(2.2) \qquad p = P_s \left(1 - \frac{t - t_a}{t_s}\right) e^{-b(t - t_a)/t_s},$$

where P_s is the peak overpressure, t_a is the time of arrival, t_s is the positive phase duration for the overpressure, and b denotes the decay coefficient.

The main advantage of this model is that the loading is applied directly to the structure subjected to the blast. There is no need to include the fluid medium in the computational domain. Since the considered time of blast is relatively short, this model seems to be good approximation of the pressures applied to the investigated surface. However, It does not account for the effects of the soil over a buried bomb or the pressure wave that travels through the surrounding air. Moreover, it does not take into account the wave reflection effects. These drawbacks cause ConWep to underestimate damage and deformation. An alternative to ConWep is the Arbitrary Lagrangian Eulerian method (ALE), which can simulate the compound effects of pressure, air, and soil [27]. While it is a more realistic modeling method, it is vastly more complex and costly and not a feasible option for the scale of this investigation. Figures below

(Fig. 2, Fig. 3) present research comparing experimental results and ConWep estimations. ConWep estimations show excellent agreement with experimental results. Since the scale of tested events in this paper is similar, ConWep is con-
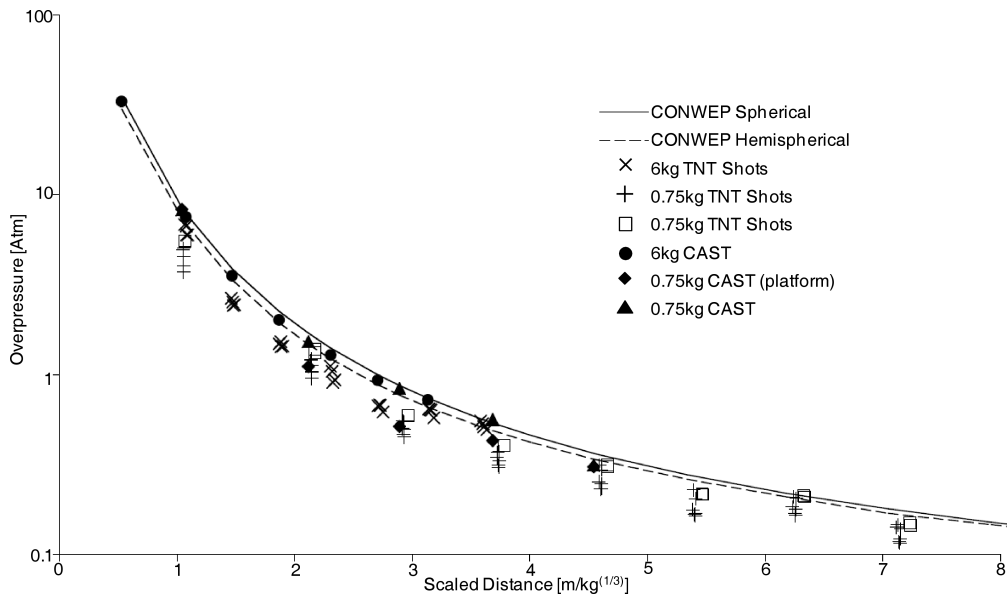
FIG. 2. Peak overpressure and shock arrival time in relation to scaled distance [16].
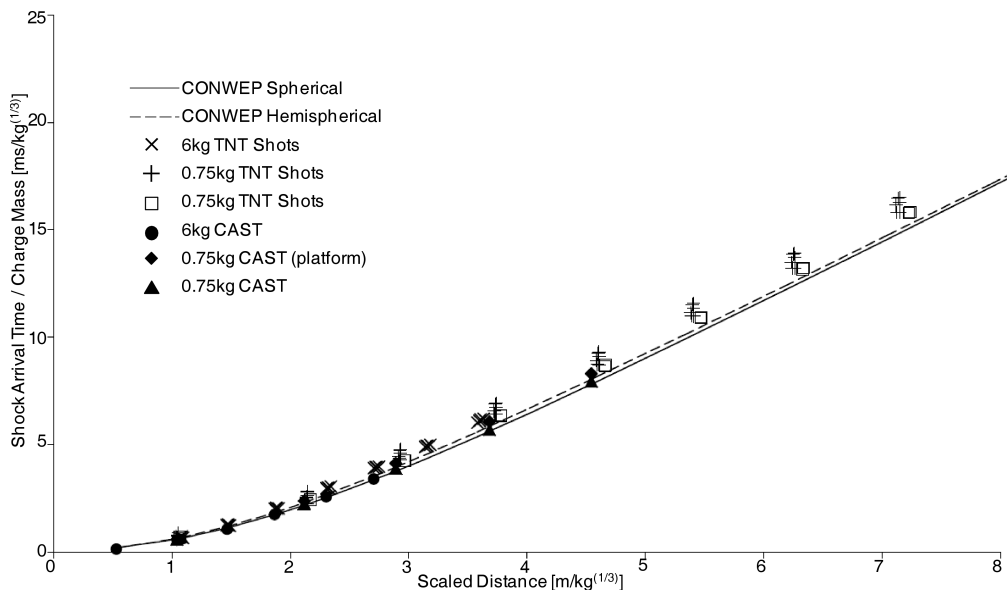
FIG. 3. Shock arrival time in relation to scaled distance [16].

sidered a very good tool for numerical modeling of the blast wave for this work purposes.

3. Material model

Steel and concrete investigated in the composite column require different material models to reflect their structural behavior both in static and dynamic load case. Concepts presented below provide simulation of material response to actions.

3.1. Steel

For both, structural and reinforcing steel the elasto-plastic model with linear hardening was employed. Essential matter is the yield criterion choice. Among many sophisticated concepts, that are available for FEM application, well proven Huber-Mises-Hencky (HMH) yield criterion was used. The HMH criterion is based on a definition of effective stress computed solely on the second deviatoric stress invariant:

$$(3.1) \qquad \overline{\sigma} = \sqrt{3J_2}.$$

The yield surface function may be presented graphically, as an infinitely long cylinder with geometric axis covering the zero hydrostatic stress axis in the principal stress space for agreed value of the hardening value. Application of equivalent stress and associated equivalent plastic strain, as internal variable of the hardening function, derives the plastic load function in the form:

$$(3.2) \qquad f = \overline{\sigma}\left(J_2\right) - H\left(\overline{\varepsilon}^{\mathrm{pl}}\right),$$

where $\overline{\sigma}$ is an equivalent stress, also known as q; H denotes the hardening function (related to effective plastic strain) describing the yield surface.

3.2. Concrete

Commonly used concrete in civil structures presents tensile strength approximately ten times lower than compressive strength. Subjected to excessive tension undergoes brittle fracture. As a result of this aforementioned HMH criterion is no longer applicable. Therefore the Drucker-Prager yield criterion [7] was used to describe concrete yield surface. It was derived as a smooth approximation of the Mohr-Coulomb Law. It consists of a modified HMH criterion, in which additional component is introduced defining pressure dependence. According to Drucker-Prager criterion, yield stress occurs when the effective stress q and hydrostatic stresses p reach their critical combination.

The linear Drucker-Prager model (Fig. 4) is used herein. It is written in terms of all three stress invariants and enables the possibility of obtaining noncircular yield surface in the deviatoric plane. In general the criterion is denoted:

$$(3.3) \qquad\qquad F = t - p \tan \beta - d = 0,$$

where d is the cohesion of the material, β is the friction angle and t is the modified effective stress. In particular, when t is equal to the equivalent stress q the yield surface is the HMH circle in the deviatoric principal stress plane. The plastic flow is described by the flow rule [7] in the form:

$$(3.4) \qquad\qquad G = t - p \tan \psi,$$

where ψ is the dilation angle, which impacts the hardening function. Herein the nonassociated flow in the $p-t$ plane is expected. If $0 \leq \psi < \beta$ the material dilates.
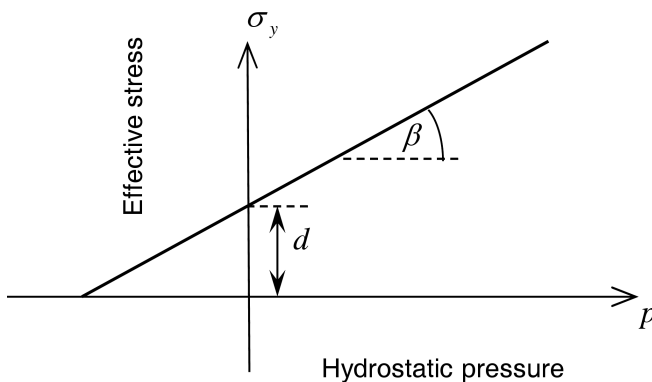
FIG. 4. Linear Drucker-Prager model in meridional plane.

4. Strain rate dependence

Material constitutive relationships vary according to the rate of loading applied to the structure. It is necessary to foresee all types of loadings (Fig. 5), that are likely to be encountered during the design lifetime. Material behavior can be affected by the loading rate but, in most cases the difference only becomes
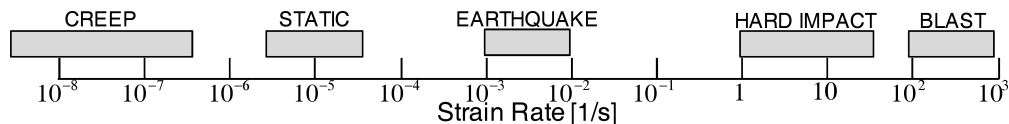
FIG. 5. Magintude of strain rates expected for different loading cases.

significant when the rate changes by more than one order of magnitude [2]. Since the blast situation is considered in this paper, strain rate dependency should not be neglected.

Many experiments proved, that materials such as concrete and steel show strength increase when the strain velocity increases. It can be noticed, that the yield limit growth is significant according to strain velocity raise, however the limit strain decreases respectively. Many methods of implementing this phenomenon to constitutive relations have been developed [14]. In general the problem may be noted in the form:

$$(4.1) \qquad s = \sigma_0\left(\bar{\varepsilon}^{\mathrm{pl}}, \theta\right) R\left(\bar{\varepsilon}^{\mathrm{pl}}, \theta\right),$$

where s is the yield stress including the strain rate dependence, σ_0 is the static yield stress and R is the nonzero strain rate stress to static stress ratio, both function of equivalent plastic strain $\left(\bar{\varepsilon}^{\mathrm{pl}}\right)$ and temperature (θ).

Standard power law of Cowper-Symonds' [5] was used for the R parameter derivation:

$$(4.2) \qquad \dot{\bar{\varepsilon}}^{\mathrm{pl}} = M(R-1)^n,$$

where $M(\theta)$ and $n(\theta)$ are temperature-dependent material parameters.

5. Damage initiation and evolution

Damage in the context of an elastic-plastic material with isotropic hardening is observed in two physical phenomena: softening of the yield stress and degradation of the elasticity. Two main mechanisms can cause the fracture of a ductile metal: ductile fracture due to the nucleation, growth, and coalescence of voids; and shear fracture due to shear band localization. Based on phenomenological observations, these two mechanisms call for different forms of the criteria.

The ductile criterion is a phenomenological model for predicting the onset of damage due to nucleation, growth, and coalescence of voids. The model assumes that the equivalent plastic strain at the onset of damage, $\bar{\varepsilon}_D^{\mathrm{pl}}$, is a function of stress triaxiality $\eta = -p/q$ and strain rate $\dot{\bar{\varepsilon}}^{\mathrm{pl}}$, where p is the pressure stress and q is the equivalent stress. The criterion for damage initiation is met when the following condition is satisfied:

$$(5.1) \qquad \omega_D = \int \frac{d\bar{\varepsilon}^{\mathrm{pl}}}{\bar{\varepsilon}_D^{\mathrm{pl}}\left(\eta, \dot{\bar{\varepsilon}}^{\mathrm{pl}}\right)} = 1,$$

where ω_D is a state variable that increases monotonically with plastic deformation. At each increment during the analysis the incremental increase in ω_D is computed as:

$$(5.2) \qquad \Delta\omega_D = \frac{\Delta\varepsilon^{\mathrm{pl}}}{\bar{\varepsilon}_D^{\mathrm{pl}}\left(\eta, \dot{\bar{\varepsilon}}^{\mathrm{pl}}\right)} \geq 0.$$

When the material exhibits strain-softening behavior, leading to strain localization, formulation in terms of stress-strain relations results in a strong mesh dependency of the FEM results. In particular, the dissipated energy decreases with the mesh size. Some mitigation of this undesirable effect is achieved in analysis introducing a characteristic length to the formulation [1, 15]. Since the softening part of the constitutive law is expressed as a stress-displacement relation, the energy dissipated during the damage process is specified per unit area, not per unit volume. This energy is treated as an additional material parameter, and it is used to compute the displacement at which full material damage occurs. This is consistent with the concept of critical energy release rate as a material parameter for fracture mechanics. This formulation ensures that the correct amount of energy is dissipated and greatly alleviates the mesh dependency.

6. Column static design

Subject of this investigation is a composite column made of circular, steel hollow section filled with reinforced concrete, which is presented in the Fig. 6. Columns are considered the most critical members for public buildings such as multi-storey car parking or an airport. Therefore in this paper a column is isolated from its primary structure and tested under assumed boundary and load conditions. The static design of such member was conducted based on the Ultimate Limit State approach recommended in the European code for steel-concrete composite structures design – Eurocode 4. As an arbitrary decision input parameters such as: materials classes, axial load, eccentricity value, column height, boundary conditions where agreed. Since the composite column static design bases on a few independent variables (e.g. steel section radius, thickness, reinforcement ratio, rebars number) there exists more than one feasible solution. Therefore, an algorithm using Matlab scripting software [28] was developed for this purpose. At first, a set of member configurations that fulfill Eurocode 4 requirements is found. Then, optimal arrangement is chosen. The decisive factor in this simple optimization is the minimum structural steel mass. This is justified by the fact, that in this sort of structural member, steel section is considered the most expensive part.

FIG. 6. Model of the reference column.

The input data for column static design are given in Table 1. Bending moment at the column head was applied in the form of eccentricity of the axial compressive force N_{Ed}. For the buckling problem analysis it is assumed, that the effective length of the column is equal to its model length, which lies on the safe side of the design. Section is designed for 90% of the load bearing capacity usage. Stirrups are taken regarding to structural requirements as $\phi 8$ loops spaced at 30 cm in the middle part of the column and 15 cm at base and head regions.

Table 1. Input data for column static design.

Column height	$H = 6.0$ m
Static load	$N_{Ed} = 1500$ kN
Bending moment	$M_{x,Ed} = 240$ kNm
	$M_{y,Ed} = 150$ kNm
Resultant load eccentricity	$e = 0.18868$ m
Steel class	S235
Concrete class	C20/25
Reinforcing steel class	BS500
Reinforcement cover	$c = 35$ mm
Required reinforcement ratio	$\rho_s = 2\%$

7. FEM NUMERICAL MODEL

Composite column which is the subject of the analyzes consists of three different materials: structural steel, concrete and reinforcing steel. Thus each has to be defined using proper finite element type and material properties to ensure most accurate simulation of the member behavior. Circular hollow section is modeled by S4R shell elements (Abaqus elements library) with four nodes and one Gauss integration point at the center of the element. For concrete C3D8R elements (Abaqus elements library) are used. It has eight-node cubic element with reduced Gauss integration at one point in the center of the element. In the Drucker-Prager material plasticity model it has to be chosen whether damage occurs due to exceeding the tension or compression stress limit. Tension criterion is defined herein, as for concrete tensile strength is much smaller, hence it is expected that damage will occur due to excessive tensile stresses. Longitudinal rebars and stirrups are modeled in Abaqus [6] using B31 beam elements with two nodes. Reinforcement is initially fully embedded in concrete, thus truss elements, i.e. T3D2 would be accurate enough for analysis. However, it is expected, that during blast situation, some parts of the reinforcement after concrete damage will be exposed and hence, bending stiffness definition (included in B31 type) of a rebar might be necessary.

Since the column is composite, proper interaction formulation is necessary. Two contact problems take place in the considered member. First is surface-to-surface contact between steel hollow section internal surface and concrete core external surface. This contact formulation is based on finite-sliding algorithm and the "hard" contact pressure-overclosure relationship [12]. Second is contact between reinforcement and concrete, which is encasing rebars and stirrups. Such contact definitions are most accurate, however the increase of computation time is significant.

Boundary conditions are simplified to the conventional approach. The base is a fixed connection as rigid joint with foundation pad, which is the most common engineering solution. Head of the column is pinned imitating joint with roof girders. It is reasonable to agree to such simplification, since the main purpose of this work is investigation composite column behavior under explosion situation. Introducing the phenomenon of joint flexibility would vastly complicate the whole problem formulation and eventually distort the results.

The analyzes conducted on numerical models of the column consist of two steps. First is static analysis applying boundary conditions, external static load and gravity to the body, in order to obtain static stress distribution. This is performed only once for each model, as it simulates the column state during its usual exploitation as a structure member. Second step is dynamic analysis in which static force and gravity is still applied to the column, however the

Table 2. Material parameters for numerical model.

		Section steel		Concrete		Reinforcement	
Mass density	[kg/m^3]	7860		2400		7860	
Isotropic Elasticity							
Young's modulus	[GPa]	310		30		210	
Poisson's ratio	[–]	0.3		0.2		0.3	
Isotropic plastic hardening H-M-H							
Yield stress	[MPa]	230	450	–		500	550
Plastic strain	[–]	0.00	0.25	–		0.00	0.25
Isotropic plastic hardening Drucker-Prager							
Angle of friction ϕ	[°]	–		65		–	
Flow stress ratio K	[–]	–		0.8		–	
Dilation angle ψ	[°]	–		45		–	
Strain rate dependence Power Law							
M	[1/s]	40		10		40	
n	[–]	5.0		3.5		5.0	
Ductile damage							
Fracture strain	[–]	10^{-1}	10^{-2}	10^{-2}	10^{-3}	10^{-1}	10^{-2}
Stress triaxiality	[–]	0.0	0.0	0.0	0.0	0.0	0.0
Strain rate	[1/s]	10^{-4}	10^{4}	10^{-4}	10^{4}	10^{-4}	10^{4}
Damage evolution linear, displacement-type							
Displacement at failure	[m]	0.01		0.001		0.01	

main load is defined as an Incident Wave using CONWEP tool. This step was conducted repeatedly, importing as Predefined Field results from static step. Parameters that were variable were the charge distance to the column and charge mass given in TNT equivalent, in order to find the minimum value of TNT needed to cause column failure.

For the dynamic step the explicit central-difference time integration rule is used. The main advantage over the implicit integration is the fact, that there is no need for finding a solution for a set of simultaneous equations, hence it requires no iterations and no tangent stiffness matrix. The basic principle of explicit method is calculating displacement, velocity and acceleration of the next increment directly, basing on previous increment data. This results in relatively inexpensive computation of each increment. Such procedure is efficient for short-time events. In this investigation the period tested was 50 ms. However there exists one important drawback. The method is conditionally stable, which means, that the time increment has to be small enough to ensure convergence of the

solution. An approximation to the stability limit is often written as the smallest transit time of a dilatational wave across any of the elements in the mesh:

$$(7.1) \qquad\qquad \Delta t \approx \frac{L_{\min}}{c_d},$$

where $L_{\min}$ is the smallest element dimension in the mesh and c_d is the dilatational wave speed. This condition is often referred to as Courant-Friedrichs-Lewy (CFL) condition [4], which describes the necessary condition for convergence while solving certain partial differential equations numerically by the method of finite differences, which are commonly used in explicit algorithms.

8. Results

8.1. Member failure criteria

Aim of the analyzes is to find TNT equivalent minimum value, for a particular designed column, which causes its failure. However, the term failure may be interpreted in different ways. Therefore, it needs to be established, what is the failure criterion. A few options are available: first is visual inspection of the damage and take an arbitrary call, whether the column is considered destroyed or not. Second approach is observation of energy existing in the column or control column head displacement. Hence, the following criteria are available:

- strain energy,
- internal energy,
- kinetic energy,
- damage dissipation energy,
- equivalent plastic strain,
- displacement of selected column points,
- visual inspection.

Analyzes showed, that the best parameters for describing member failure are column head vertical displacement, kinetic energy and damage dissipation energy. Damaged column is still subjected to gravity and the structure dead load. This causes further increase of displacements and velocity, which is directly connected with kinetic energy. For a member that endured the blast event, one can observe stabilization of the displacements on certain level. Moreover, the kinetic energy decreases leading to the conclusion, that the member tends to go back to its primary configuration. Analyzing the damage dissipation energy, it can be estimated, what amount of the total energy caused material fracture eliminating the most exhausted FEM elements.

Figures 7 and 8 below show comparison of undamaged and destroyed columns. Energy and displacement plots show clearly the characteristics mentioned above.
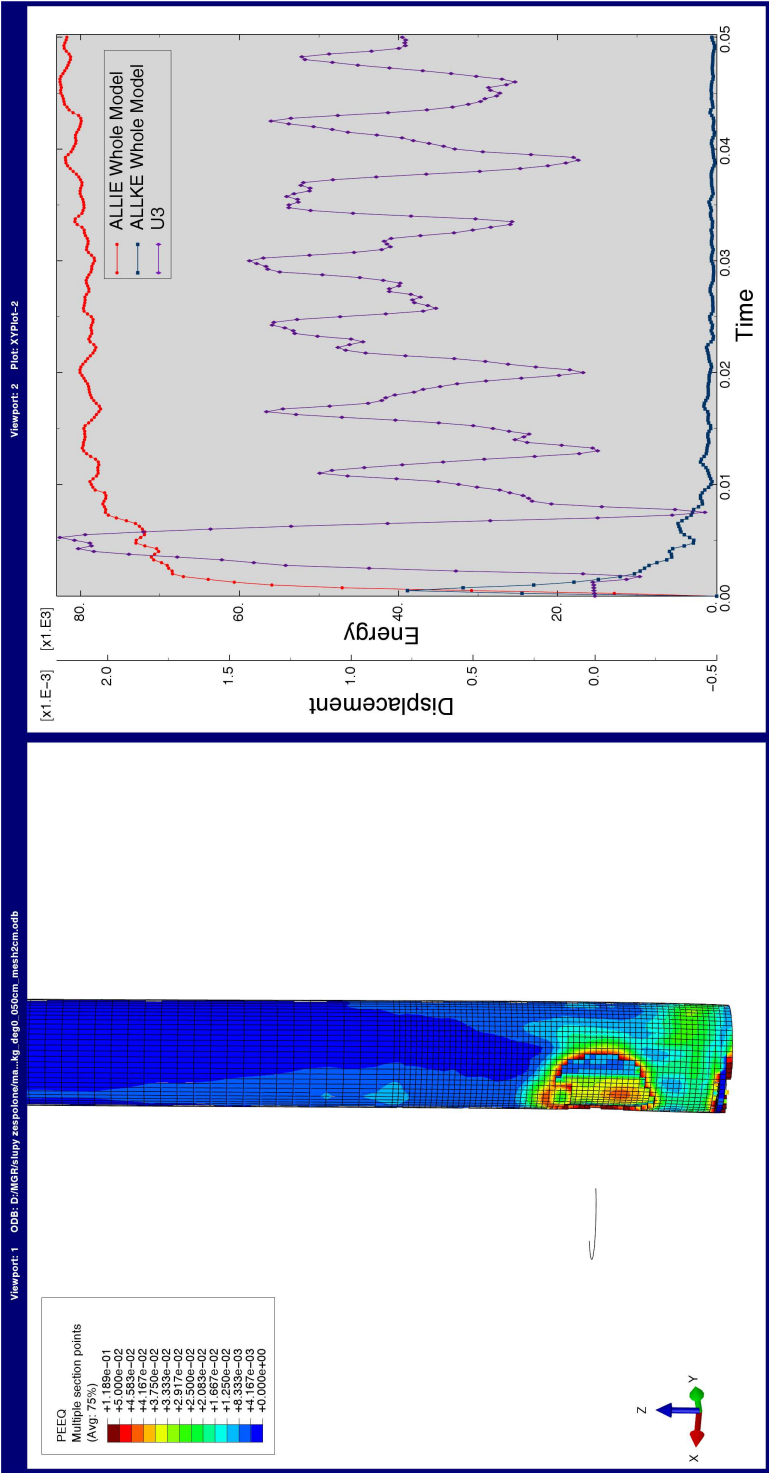
FIG. 7. Undamaged column – view without steel section, energy and displacement plot: (left) equivalent plastic strain at time 0.05 s, (right) model energies and column tip displacement curves.
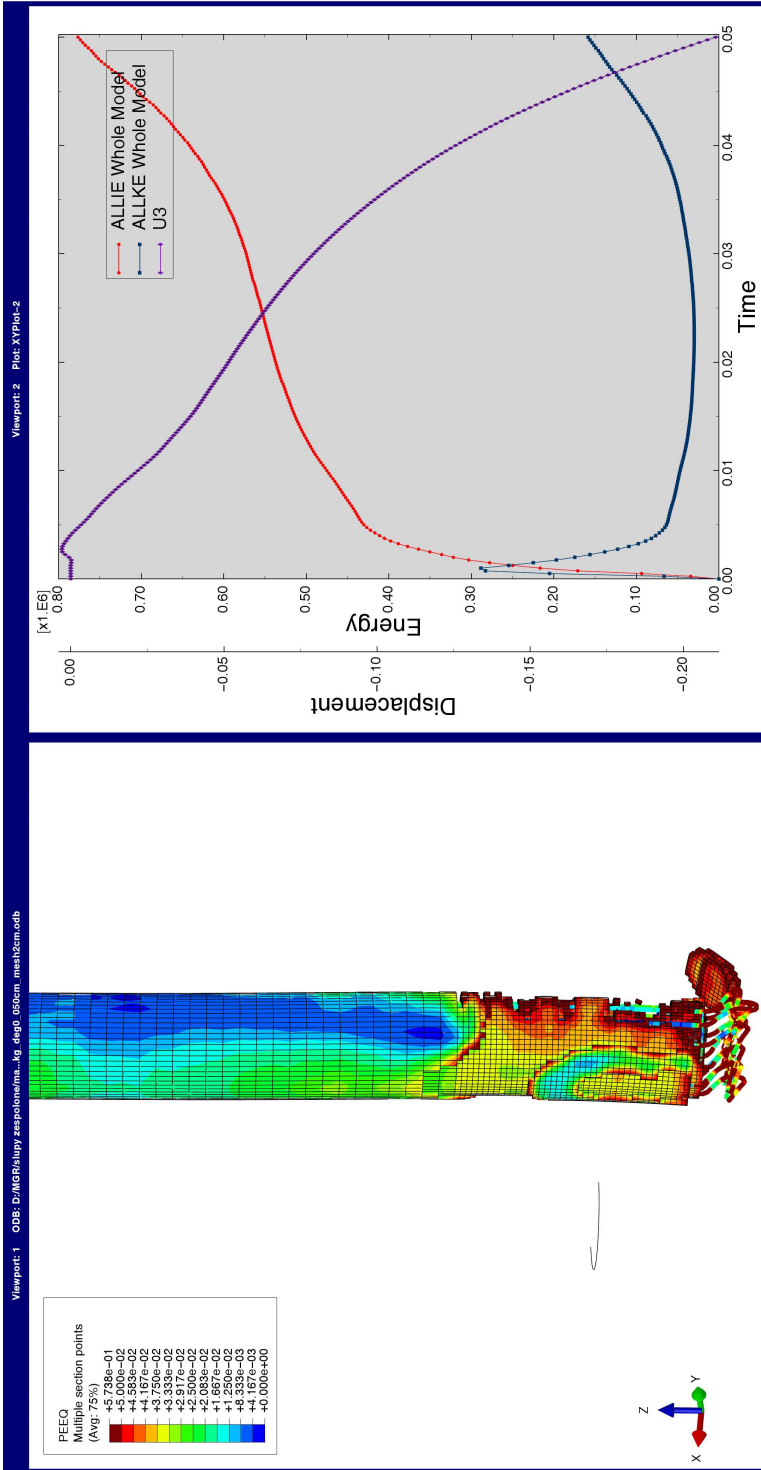
Fig. 8. Destroyed column – view without the steel section, energy and displacement plot: (left) equivalent plastic strain at time 0.05 s, (right) model energies and column tip displacement curves.

View of the steel section has been removed from these figures to visualize the state of the concrete core, in which damage is much more greater and occurs faster than in structural steel.

8.2. Reference column: results

The column designed as described before in chapter 6 was subjected to multiple analyzes with the TNT charge at three different distances: 0.5 m, 1.0 m and 2.0 m from the external surface of the column. The CONWEP model was set with properties modeling a surface blast, where the influence of blast wave reflection and self-amplification is taken into account. The charge was modeled at the level of 0.5 m above the column base, which is assumed to be the floor level in a building. Conducted analyzes present the least TNT mass of what would lead the member to failure according to criteria established before. Results printed in Table 3 show, that increasing the distance of charge placement, reduces immensely the destructive effects of blast event. The scaled distance parameter as per (1) proves, that the overpressure peak value of blast wave decreases as the wave travels, even though the influence of the medium flow is neglected in the analysis.

Table 3. Analysis results for the reference column.

Distance [m]	Charge mass [kg]	Scaled distance Z [m/kg$^{(1/3)}$]
0.5	27	0.1667
1.0	110	0.2087
1.5	227	0.2459
2.0	330	0.2894

The failure mechanism of investigated member presents interesting structure response. The most sharp and expressive effect is totally damaged slice of concrete core of approximately 15–20 cm width. This means, that for these particular concrete finite elements the excessive tensile stress was reached. After the local damage initiation, further strain increase leads to the damage evolution. Eventually, ultimate strain limit is reached, at which full material damage occurs. In that case the element is excluded from the analyzes, as it can no longer sustain or transfer any stresses. On the other hand, the external steel section, basing on visual inspection only, seems to be in good condition. Checking the equivalent plastic strain one can notice, that few elements have exceeded the value of 5%. This means, that probably the structural steel might serve still as a part of the building structure.

The explanation to such member behavior lies in the event nature. Abrupt overpressure peak applied to the external member surface induces sophisticated type of load. The pressure wave travels through the structure causing locally high internal stress of both signs in very short time. Moreover, the phenomenon of internal reflection appears on the connection between steel section and concrete core. Since the concrete core is of approximately seven times lower stiffness, the blast wave is reflected inwards repeatedly. Hence the concrete core having its tensile strength ten times lower than compressive strength yields first due to brittle fracture.

8.3. Strengthening solutions

The main aim of this work is to find solutions, how to increase the safety of the column during an explosion. Below are proposed a few options of improving composite column section strength in terms of resistance to blast load.

One of the ideas is to design the column assuming less usage ratio of load bearing capacity. It is based on the assumption, that stronger section in terms of static load resistance will be also more resistant to explosions. The static design was conducted again as described in Sec. 6 with the same input data, but with the usage parameter decreased by 30%. Table 4 presents output results for static

Table 4. Strengthened sections dimensions.

Case	Steel section diameter d [mm]	Steel section thickness t [mm]	Rebars number n [–]	Rebars diameter ϕ [mm]	Composite section factor δ [–]	Steel yield limit f_y [MPa]	Concrete tensile strength f_{ctk} [MPa]
Reference column	406.4	8.0	12	16	0.4835	235	3.0
60% load capacity used	508.0	6.0	8	25	0.3541	235	3.0
30% load capacity used	610.0	8.8	8	30	0.4030	235	3.0
Double pipe thickness 16 mm	406.4	16.0	12	16	0.6067	235	3.0
Higher steel class S355	406.4	8.0	12	16	0.5532	355	3.0
Higher concrete class C40/50	406.4	8.0	12	16	0.3579	235	4.6
Increase of reinforcement	406.4	8.0	12	25	0.4277	235	3.0

design with the load bearing capacity usage of 90%, 60%, 30% respectively and the further proposals described below.

Next proposals are based on improving particular elements of the section. First, very simple concept of thickening the steel section maintaining its design diameter. The thickness of 16 mm is twice as big as the original value. This solution might be easily implemented in practice as it involves only choosing thicker profile. Second, taking into the design higher steel grade – from S235 to S355 – results in increasing the steel yield stress limit by 50%. Next, increasing the concrete class from C20/25 to C40/C50 in general doubles its most important properties such as compressive and tensile strength. Also increase by 17% of the previous value in concrete stiffness modulus is observed. The solution is easy to implement, as it is not associated with any changes of dimensions of the member. The last but not least proposal is increasing of the longitudinal reinforcement. Conversion from 12ø16 to 12ø25 gives the effect of doubling the reinforcement ratio in this particular design. It is assumed that stronger reinforcement can overtake more destructive tensile stresses from the concrete core.

Results of analyzes performed on improved models are summarized in comparison with the reference column. Table 5 presents the increase in minimum charge mass value causing failure referring to the results from Table 4.

Table 5. Results summary.

Distance between column surface and charge position	Increase of minimum charge mass causing column failure			
	0.5 m	1.0 m	2.0 m	Average Δ_{TNT}
	[–]	[–]	[–]	[–]
Reference column	1.0000	1.0000	1.0000	**1.0000**
60% load capacity used	1.0000	0.9818	0.9091	**0.9636**
30% load capacity used	1.3333	1.4182	1.3333	**1.3616**
Double pipe thickness 16 mm	1.3333	1.5455	1.3152	**1.3980**
Higher steel class S355	1.0741	1.1091	1.1515	**1.1116**
Higher concrete class C40/50	1.0370	1.1273	1.1455	**1.1033**
Increase of reinforcement to 12ø25	1.1111	1.2727	1.1515	**1.1785**

The case of 60% load bearing capacity usage shows effect totally opposite to the desired result. Instead of growth, a decrease in minimum damaging charge mass is observed. The new section turns out to be more vulnerable than the reference one in terms of blast resistance. This proves the fact, that resistance to static loads is not directly related to dynamic load resistance. Although the section is thicker by 25%, the steel pipe thickness is smaller than in previous
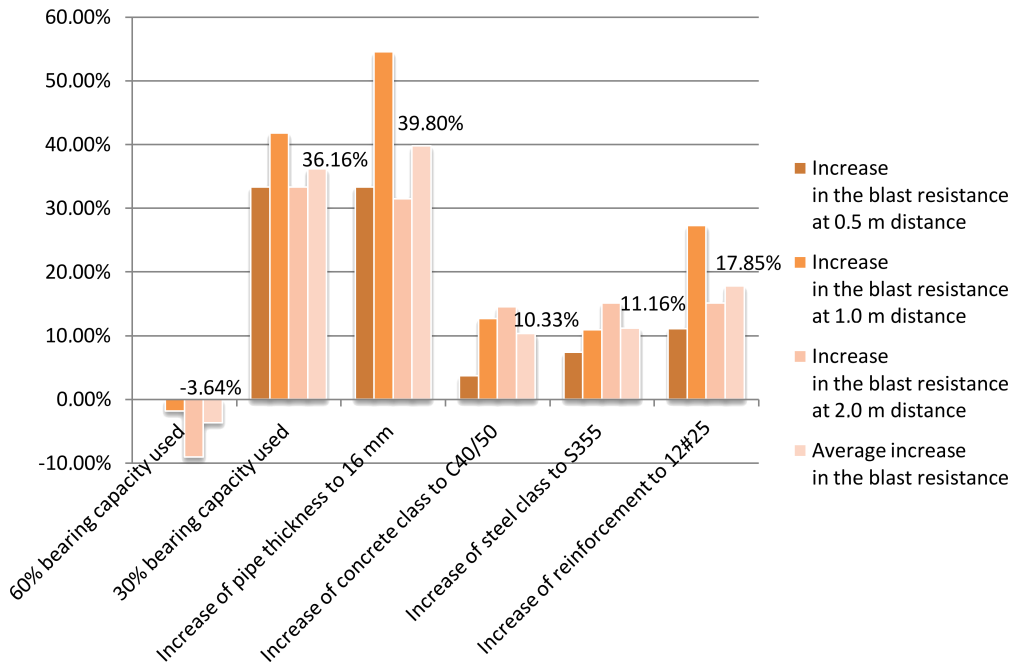
Fig. 9. Breakdown of blast resistance increase for different strengthening solutions.

configuration by 2 mm. This might be explanation for poorer performance during blast event. Steel can endure more severe dynamic actions due to its ductile properties. On the other hand, concrete is a brittle material. Therefore, introducing more concrete to the section does not improve blast resistance. Designing a case with 30% load capacity usage introduces significant increase in explosion resistance, however member dimensions grow severely, what causes too big expenses for the structure. Moreover, such big column diameter enlarge interferes with architectural concept of a building, which can disqualify the solution as well.

After doubling the steel profile thickness nearly 40% in average of blast resistance increase is a promising result, therefore this solution may be seriously taken into account in practice. The only drawback is twice as big the structural steel mass and hence, the cost of member production grows significantly. The case of introducing higher steel grade brings results, which are not very satisfactory, as 11.16% in average is not very significant growth. The section with higher concrete class, is not very advantageous for the member in terms of blast resistance. This proves again, that concrete is the weakest component of the member. Introducing double reinforcement ratio replacing the 12ø16 with 12ø25 returned results showing that this concept is justified to be used in practice.

It was expected, that strength results would occur proportional to the value of the distance of the charge ignition. Instead, the relative increases expressed in % in Table 4 indicate lack of such relation. However, Table 3 presents linear relation between the Scaled distance Z parameter for each case. This leads to the conclusion, that the Z value enables comparing blast effects more objectively than simple minimum charge mass value or simple relative increases expressed in percentages.

Furthermore, the value of minimum charge mass causing the member failure is not a sufficient parameter for comparing different members due to economical reasons. For example, the case of design with 30% load capacity used significantly enlarges mass of the member and such drawback needs to be properly accounted for. The idea is to merge the advantage of higher blast resistance and the disadvantage of higher concrete or steel mass (8.3, 8.3) into one coefficient defined herein as the blast strengthen efficiency parameter given in equation below:

$$(8.1) \qquad \eta = \frac{\Delta_{TNT}}{\Delta_E},$$

$$(8.2) \qquad \Delta_E = \frac{P^{(i)}}{P^{ref}},$$

$$(8.3) \qquad P^{(i)} = M_s^{(i)} P_{u,s}^{(i)} + V_c^{(i)} P_{u,c}^{(i)} + M_r^{(i)} P_{u,r}^{(i)},$$

where Δ_{TNT} is the relative charge mass increase and Δ_E is the column material price increase comparing to the reference member price. It is calculated using average unit prices in Poland of steel, concrete and reinforcement $P_{u,s}^{(i)}$, $P_{u,c}^{(i)}$, $P_{u,r}^{(i)}$ from the fourth quarter of 2012, gathered in pricing books the "Sekocenbud" series.

The strengthening efficiency factor η values reveal the correlation between increasing member blast resistance and the drawbacks of increasing its dimensions. Higher material costs of improved members present the impact of the economical circumstances on the investigated problem. Nevertheless, due to variability of prices caused by criteria such as location, transportation, etc., it has been simplified to the shape in Eq. (8.1).

Table 6 shows clearly the drawbacks of enlarging the column in the concept of higher static load capacity. The case of 30% member returned the second highest resistance increase of 36.16%. However, the steel and concrete usage would consume the benefits of implementing this solution, which makes it inefficient. On the other hand, the case of higher steel class seems to be the most reasonable solution, though as it has been mentioned before, exact material prices may vary according to specific location etc.

Table 6. Strengthening efficiency factor for proposed members.

Case	Estimated column price	Relative price increase	Charge mass increase	Strengthening efficiency factor
	P [EUR]	Δ_E [–]	Δ_{TNT} [–]	η [–]
Reference column	466.01	1.0000	1.0000	**1.0000**
60% load capacity	567.62	1.2180	0.9636	**0.7911**
30% load capacity	899.24	1.9296	1.3616	**0.7056**
Double pipe thickness	728.27	1.5628	1.3980	**0.8946**
Higher steel class	477.48	1.0246	1.1116	**1.0849**
Higher concrete class	490.73	1.0530	1.1033	**1.0477**
Increase of reinforcement	667.48	1.4323	1.1785	**0.8228**

9. CONCLUSIONS

Although military facilities, skyscrapers, nuclear power plants and dams are designed to resist explosive loads, the majority of public buildings is vulnerable to terrorist attacks, least because of lack of estimation of explosion situation effects. Even a small amount of charge placed in critical point can cause very serious damage. There exists a need to provide solutions how to protect structures against blasts, both, newly designed objects, as well as improve the safety of already existing ones.

The column failure mechanism occurs to be fairly complex. It is not possible to choose one criterion to determine whether the member is considered destroyed or not. It is a combination of different energy types in the material, its velocity, displacement and expected equilibrium state. Especially in the case of composite columns there exists the threat of underestimating the damage. Even though steel section may look stable, the concrete core may be subjected to large fracture.

Among the proposed strengthening solutions the concepts of increasing static load capacity turned out to be unsuccessful. Economical drawbacks of these changes consume the benefits in blast resistance. Analyzes lead to the conclusion, that the most promising ideas are connected with improving the steel section performance, both increasing its thickness and the limit yield stress gave good results.

As a final remark it may be noted, that more attention to explosion load has to be brought during the design procedure of buildings. Design codes used in Europe mention about taking into consideration possible explosions during load collecting and instructs to treat it as an accidental situation. However, it does

not provide the user with any guidance how to estimate and model the effects of a blast event. This raises the need to address this deficiency.

References

1. BAZANT Z.P., *Concrete fracture models: Testing and practice*, Engineering Fracture Mechanics, **69**, 165–205, 2001.

2. BISCHOFF P.H., PERRY S.H., *Compressive behaviour of concrete at high strain rates*, Materials and Structures, **24**, 425–450, 1991.

3. CHOCK J.M.K., KAPANIA R.K., *Review of two methods for calculating explosive air blast*, Shock and Vibration Digest, **33**, 91–102, 2001.

4. COURANT R., FRIEDRICHS K., LEWY H., *On the partial difference equations of mathematical physics*, IBM Journal of Research and Development, **11**, 215–234, 1967.

5. COWPER G.R., SYMOND P.S., *Strain Hardening and Strain Rate Effects in the Impact Loading of Cantilever Beams*, Applied Mathematics Report No. 28, Brown University, Providence, Rhode Island, USA, 1957.

6. Dassault Systemes, Abaqus 6.11 Documentation, 2011.

7. DRUCKER D.C., PRAGER W., *Soil mechanics and plastic analysis or limit design*, Quart. Appl. Math., **10**, 157–165, 1952.

8. GAJEWSKI T., GARBOWSKI T., *Calibration of concrete parameters based on digital image correlation and inverse analysis*, Archives of Civil and Mechanical Engineering, **14**, 1, 170–180, 2014.

9. GAJEWSKI T., GARBOWSKI T., *Mixed experimental/numerical methods applied for concrete parameters estimation*, Proceedings of XX International Conference on Computer Methods in Mechanics CMM2013, Recent Advances in Computational Mechanics, T. Łodygowski, J. Rakowski, P. Litewka [Eds.], 293–302, CRC Press, 2014.

10. GARBOWSKI T., MAIER G., NOVATI G., *Diagnosis of concrete dams by flat-jack tests and inverse analyses based on proper orthogonal decomposition*, Journal of Mechanics of Materials and Structures, **6**, 1–4, 181–202, 2011.

11. GEORGIN J.F., REYNOUARD J.M., *Modeling of structures subjected to impact: Concrete behaviour under high strain rate*, Cement and Concrete Composites, **25**, 131–143, 2003.

12. GOYAL S., PINSON E.N., SINDEN F.W., *Simulation of dynamics of interacting rigid bodies including friction I: General problem and contact model*, Engineering with Computers, **10**, 162–174, 1994.

13. GURSON A.L., *Continuum Theory of Ductile Rupture by Void Nucleation and Growth: Part I – Yield Criteria and Flow Rules for Porous Ductile Materials*, Journal of Engineering Materials and Technology, 99, 2–15, 1997.

14. HERV G., GATUINGT, F., IBRAHIMBEGOVI A., *On numerical implementation of a coupled rate dependent damage-plasticity constitutive model for concrete in application to high-rate dynamics*, Engineering Computations (Swansea, Wales), **22**, 583–604, 2005.

15. HILLERBORG A., MODEER M., PETERSSON P.E., *Analysis of Crack Formation and Crack Growth in Concrete by Means of Fracture Mechanics and Finite Elements*, Cement and Concrete Research, **6**, 773–782, 1976.

16. Huntington-Thresher W., Cullis I.G., *TNT blast scaling for small charges*, Proceedings of 19th Int. Sym. on Ballistics, Interlaken, Switzerland, 647–654, 2001.

17. Kingery C.N., Bulmash G., *Airblast parameters from TNT spherical air burst and hemispherical surface burst*, Technical Report ARBRL-TR-02555, U.S. Army Ballistic Research Laboratory, 1984.

18. Lee J., Fenves G.L., *Plastic-damage model for cyclic loading of concrete structures*, Journal of Engineering Mechanics, **124**, 892–900, 1998.

19. Lubliner J., Oliver J., Oller S., Oate E., *A plastic-damage model for concrete*, International Journal of Solids and Structures, **25**, 299–326, 1989.

20. Zirpoi A., Novati G., Maier G., Garbowski T., *Dilatometric tests combined with computer simulations and parameter identification for in-depth diagnostic analysis of concrete dams*, Proceedings of the International Symposium on Life-Cycle Civil Engineering IALCCE '08, CRC Press, 259–264, 2008.

21. McAllister T.P., Gross J.L., Sadek F., Kirkpatrick S., MacNeill R.A., Zarghamee M., Erbay O.O., Sarawit A.T., *Analysis of structural response of WTC 7 to fire and sequential failures leading to collapse*, Journal of Structural Engineering, **138**, 1, 109–117, 2012.

22. Neuberger A., Peles S., Rittel D., *Scaling the response of circular plates subjected to large and close-range spherical explosions. Part II: Buried charges*, International Journal of Impact Engineering, **34**, 874–882, 2007.

23. Ngo T., Mendis P., Gupta A., Ramsay J., *Blast loading and blast effects on structures – An overview*, Electronic Journal of Structural Engineering, **7**, 76–91, 2007.

24. Rodriguez-Nikl T., Lee C.-S., Hegemier G.A., Seible F., *Experimental performance of concrete columns with composite jackets under blast loading*, Journal of Structural Engineering, **138**, 1, 81–89, 2012.

25. Ross C. Allen, Thompson P.Y., Tedesco J.W., *Split-Hopkinson pressure-bar tests on concrete and mortar in tension and compression*, ACI Materials Journal, **86**, 475–481, 1989.

26. Rule W.K., Jones S.E., *A Revised Form for the Johnson-Cook Strength Model*, International Journal of Impact Engineering, **21**, 609–624, 1989.

27. Soutis C., Mohamed G., Hodzic A., *Modelling the structural response of GLARE panels to blast load*, Composite Structures, **94**, 267–276, 2011.

28. The MathWorks, Inc., Matlab R2011a Documentation, 2011.

The 8th WORKSHOP

DYNAMIC BEHAVIOUR OF MATERIALS AND ITS APPLICATIONS IN INDUSTRIAL PROCESSES

Warsaw, 25 – 27 June, 2014

Institute of Fundamental Technological Research
Polish Academy of Sciences

Co-organized by

General

Within the last years, a consortium of Universities and Research Centers including the University Carlos III of Madrid, the National Engineering School of Metz, the Poznan University of Technology and the Institute of Fundamental Technological Research of the Polish Academy of Sciences, Warsaw, have been organizing an annual International Workshop devoted to the dynamic behaviour of materials. The Workshop is conducted with the collaboration of DYMAT Association.

Invited Lectures

Alexis Rusinek

(National Engineering School of Metz) – opening lecture:
Discussion about friction effect under quasi-static and dynamic loading, modelling and applications

Krzysztof Gałka, Aleksander Gałka

(EXPLOMET High – Energy Techniques Works):
Explosive cladding of metals technology – selected aspects of industrial application

Kinga Nalepka

(AGH University of Science and Technology):
Modeling microstructure of copper-sapphire nanocomposite

Wojciech Sumelka

(Poznan University of Technology):
Fractional calculus for continuum mechanics – theory, applications and future task

Conference Site

Conference will take place in the Mirrors Room at Staszic Palace, Nowy Świat 72, Warsaw.

Staszic Palace

The bronze statue of astronomer Nicolaus Copernicus holding a compass and armillary sphere designed by Bertel Thorvaldsen in 1822 and erected in 1828–30 was funded by public donations and by the scientist and philosopher

Stanisław Staszic. The Warsaw Community region includes historic municipalities such as Royal Castle and birthplace of Fryderyk Chopin in Zelazowa Wola (http://www.um.warszawa.pl/en).

Birthplace of Fryderyk Chopin
in Zelazowa Wola

Monument to Fryderyk Chopin
in Zelazowa Wola

Scientific Committee

A. Arias	(UC3M-Spain)	J. Małachowski	(MUT-Poland)
Z. Azari	(ENIM-France)	H. Miguélez	(UC3M-Spain)
J. Fernández-Sáez	(UC3M-Spain)	Z. Nowak	(IPPT-Poland)
A. Glema	(PUT-Poland)	J. Pernas-Sánchez	(UC3M-Spain)
S. Hiermaier	(EMI-Germany	R. Pęcherski	(IPPT-Poland)
	– President of DYMAT)	J. Rodriguez-Martinez	(UC3M-Spain)
Z. Kowalewski	(IPPT-Poland)	A. Rusinek	(ENIM-France)
P. Lipinski	(ENIM-France)	G. Vadillo	(UC3M-Spain)
T. Łodygowski	(PUT-Poland)	R. Zaera	(UC3M-Spain)

Chairmen

R. Pęcherski	(IPPT PAN)
Z Nowak	(IPPT PAN)
W. Moćko	(IPPT PAN) – Scientific Secretary

Local Organizing Committee

M. Nowak	(IPPT PAN Warsaw)
L. Frąś	(IPPT PAN Warsaw)
K. Nalepka	(AGH Krakow)

Preliminary Conference Programme

Registration will begin on Wednesday, June 25, at 8.30 a.m. at the Conference site. Opening Session will start, June 25, at 10.00 a.m.

Gala Dinner: Thursday, June 26 at 8 p.m.

The conference closure is planned on Friday, June 27 after lunch 15.00 p.m

Abstracts

Abstracts should be submitted electronically on-line via the Conference website or via mail to **workshop2014@ippt.pan.pl**. Guidelines are available at the Conference website

> http://workshop2014.ippt.pan.pl/Abstracts.html

A book of abstracts will be distributed to participants during the conference.

Publications

We will encourage all the authors to submit **full length papers** after the conference for publication according to a usual peer review procedure in *Engineering Transactions*

> http://et.ippt.pan.pl/

Conference fee

Registration fee includes: participation in all sessions, coffee breaks, lunches, conference materials and gala dinner

Standard registration fee:
> 1350 PLN + 23% VAT = 1661 PLN

There exists fee reduction for Dymat members

Dymat members registration fee:
> 1250 PLN + 23% VAT = 1538 PLN

Detailed information concerning the payment procedure are available on the *Workshop Warsaw 2014 web page*

> http://workshop2014.ippt.pan.pl/Registration.html

Travel and accommodation

Hotel reservations at preferential rates will be arranged by the organizers. Detailed information will be available in due time on the *Workshop Warsaw 2014 web page*

> http://workshop2014.ippt.pan.pl

Contact

For further information please do not hesitate to contact us:

Workshop Warsaw 2014
Institute of Fundamental Technological Research
Pawińskikiego 5B, 02-106 Warszawa, Poland
fax: +48 22 826 98 15
Chairmen of the Conference
e-mail: rpecher@ippt.pan.pl
            znowak@ippt.pan.pl

Conference Partner

Nowogrodzka 62B lok. 22
02-002 Warszawa, Poland
tel.: +48 22 870 09 33
fax: +48 22 628 94 61
http://www.globalwings.pl

39ᵗʰ Solid Mechanics Conference

September 1–5, 2014
Zakopane, Poland

General The Solid Mechanics Conferences have been organized by the Institute of Fundamental Technological Research since 1953. The Conferences have maintained high scientific standard and served as a forum for the exchange of ideas and research information. Traditionally, invited lectures have been presented by outstanding researchers at these Conferences. The aim of the Conference is to bring together researchers from different countries and to create for them the possibility for the presentation and discussion of scientific results from a wide area of solid mechanics.

Thematic Sessions and Chairmen:

Micromechanics, Interfaces and Multi-Scale Modelling
    S. Meguid (Canada) & H. Petryk (Poland)

Fracture, Damage and Fatigue of Materials
    D.R. Hayhurst (UK) & Z. Nowak (Poland)

Continuum Mechanics, Elasticity and Plasticity
(Special Session in Memory of Prof. Piotr Perzyna)
    H. Altenbach (Germany), B. Skoczeń (Poland) & R. Pęcherski (Poland)

Experimental Mechanics (Special Session in Memory of Prof. Wojciech Szczepiński)
    N. Gupta (India) & A. Rusinek (France)

Mechanics of Composites, Porous Media
    P. Kowalczyk (Poland) & J. Rojek (Poland)

Geomechanics
    Z. Mróz (Poland), S. Pietruszczak (Canada) & J. Tejchman (Poland)

Smart Materials and Structures
    H. Tobushi (Japan) & E. Pieczyska (Poland)

Structural Mechanics, Optimization and Reliability Analysis
    J. Holnicki-Szulc (Poland) & T. Szolc (Poland)

Shells and Plates
  W. Pietraszkiewicz (Poland) & K. Wiśniewski (Poland)

Computational Aspects of Solid Mechanics
  J. Eberhardsteiner (Austria) & T. Burczyński (Poland)

Dynamics of Solids and Structures
  R. Iwankiewicz (Germany) & Z. Kotulski (Poland)

Invited Plenary Lectures:

HOLM ALTENBACH, Germany
  Mechanics of Nanostructures

JOSEF EBERHARDSTEINER, Austria
  Mechanical Behavior of Wood – a Bridge from Microstructure to Structural Applications by Means of Computational Methods

NARINDER GUPTA, India
  Some Aspects of Large Deformations of Structures under Dynamic Loading

DAVID HAYHURST, UK
  High-temperature Continuum Damage Mechanics. Simulation of Materials and Components from Processing and Manufacture to Component Performance

SHAKER MEGUID, Canada
  Multiscale Modelling of Multifunctional Nanocomposites for Aerospace Applications

RYSZARD PĘCHERSKI, Poland
  Plastic Flow and Failure of Solids. Modelling Across Scales

KRZYSZTOF WIŚNIEWSKI, Poland
  Recent Improvements in Mixed/Enhanced Shell Elements with Drilling Rotation

RAMON ZAERA POLO, Spain
  Deformation of Dynamically Phase Transforming Metals in Adiabatic Conditions: Thermal Effects and Instabilities

Contact: Institute of Fundamental Technological Research
        phone: +48 22 826 98 34   fax: +48 22 826 73 80
        e-mail: solmech2014@ippt.pan.pl

Further informations & guidelines will be available at the Conference site:
www.solmech2014.ippt.pan.pl